Evidence of microbial activity from a shallow water whale fall (Voghera, northern Italy)

S. Danise, B. Cavalazzi, S. Dominici, Frances Westall, S. Monechi, S. Guioli

Evidence of microbial activity form a Miocene shallow water whale fall (Voghera, northern Italy)

S. Danise[1,2]*, B. Cavalazzi[3,4], S. Dominici[5], F. Westall[3], S. Monechi[1], S. Guioli[6]

[1] Dipartimento di Scienze della Terra, Università degli Studi di Firenze, via La Pira 4, 50121, Firenze, Italy.

[2] Present address: School of Geography, Earth and Environmental Sciences, University of Plymouth, Drake Circus, Plymouth, Devon, PL4 8AA, United Kingdom.

[3] Centre de Biophysique Moléculaire, CNRS, Rue Charles Sadron, Orléans cedex 2, 45071, France.

[4] Department of Geology, University of Johannesburg, Kingsway Campus, PO Box 524 Auckland Park, 2006 South Africa.

[5] Museo di Storia Naturale, Sezione di Geologia e Paleontologia, Università degli Studi di Firenze, via La Pira 4, 50121, Firenze, Italy.

[6] Civico Museo di Scienze Naturali di Voghera, Via Gramsci 1, 27058 Voghera, Pavia, Italy.

*corresponding author. Tel: +44 (0)1752 584874. E-mail : silvia.danise@plymouth.ac.uk

ABSTRACT

The fossil bones, associated carbonate cements and enclosing concretion of a Miocene mysticete from inner shelf deposits (Monte Vallassa Formation, northern Italy) were analyzed for evidence of microbial activity. Optical and scanning electron microscopy, Raman spectroscopy, and stable C

and O isotope geochemistry were used for high spatial resolution microfacies and biosedimentological analyses. Whale cancellous bones were filled by different carbonate cements including microcrystalline dolomite, rhombohedral dolomite and sparry calcite. Biofabric and biominerals such as microbial peloids, clotted textures and pyrite framboids were associated with the dolomite cements. Dolomite inside cancellous bones and in the enclosing concretion showed similar isotopic values (avg $\delta^{13}C$: -7.12 ‰; avg $\delta^{18}O$: +3.81 ‰), depleted with respect to the (late) sparry calcite cement (avg $\delta^{13}C$: -0.55 ‰; avg $\delta^{18}O$: -0.98 ‰). Microcrystalline barite ($BaSO_4$) was observed on the external surface of the bones. In addition, two different types of microborings were recognized, distinguished by their size and morphology and were ascribed respectively to prokaryote and fungal trace makers. Our results testify for the development of a diverse microbial ecosystem during the decay of a shallow water whale carcass, which could be detected in the fossil record. However, none of the observed biosignatures (*e.g.,* microbial peloids, clotted textures) can be used alone as a positive fossil evidence of the general development of a sulfophilic stage of whale fall ecological succession. The occurrence of the hard parts of chemosynthetic invertebrates associated with fossil whale bones is still the more convincing proof of the development of a sulfide-base chemoautotrophic ecosystem.

KEYWORDS: whale fall; microbial activity; carbonate biofabrics; microborings.

1. Introduction

Dead whales sunk to the deep sea floor create persistent and ecologically significant habitats that can support a diverse and highly specialized community (Smith, 2006). Sharks, hagfishes and other scavenging organisms remove flash and soft tissues (“mobile scavenger stage”), polychaetes,

51 crustaceans and other opportunistic small-sized animals thrive on whale organic remains
52 ("enrichment opportunist stage"), while a long lasting and complex community relies on the
53 hydrogen sulfide (H_2S) and other chemical compounds produced by microbial consumption of the
54 lipid-rich bones ("sulfophilic stage"; Smith and Baco, 2003). In modern oceans the sediments
55 beneath and around whale carcasses, progressively enriched with lipids and other organic
56 compounds (Naganuma et al., 1996; Smith et al., 1998), experience anoxic conditions due to high
57 microbial oxygen consumption that favors anaerobic processes such as sulfate reduction and
58 methanogenesis (Allison et al., 1991). Whale carcasses and the surrounding sediments represent
59 thus a suitable habitat for sulfide-based chemosynthetic communities as well as sulfate-reducing
60 and methane-producing microbial consortia (Goffredi et al., 2008; Treude et al., 2009).
61 Chemosynthetic microorganisms found at deep water whale falls include free-living, sulfur-
62 oxidizing bacteria (*e.g., Beggiatoa* spp.) which cover the bones and the adjacent sediment surfaces,
63 and symbiotic bacteria associated with bivalves and tube-worms (Bennett et al., 1994; Deming et
64 al., 1997; Goffredi et al., 2004). Vesicomyid clams, bathymodioline mussels, and vestimentiferan
65 tube-worms, together with their associated microbial consortia, constitute symbiont-dominated
66 oases similar to those occurring at hydrocarbon seeps and hydrothermal vents (Dubilier et al.,
67 2008).
68 Macrofaunal ecosystems around whale falls have been recognized in the fossil record as far
69 back as the late Eocene (Kiel and Goedert, 2006); an age coincident with the evolution of the first
70 large ocean-going whales (Kiel and Little, 2006). In the last two decades most of the studies were
71 concentrated on the macrofaunal component of fossil whale fall communities, represented mainly
72 by fossil chemosynthetic bivalves or bacterial mat-grazing gastropods found in close association
73 with whale bones (Squires et al., 1991; Hachiya, 1992; Goedert et al., 1995; Amano and Little,
74 2005; Nesbitt, 2005; Kiel and Goedert, 2006; Amano et al., 2007; Pyenson and Haasl, 2007;
75 Dominici et al., 2009; Danise et al., 2010; Kiel et al., 2010; Higgs et al., 2011). Only in a few cases

76 has the attention focused on the traces left in the fossil record by the microbial component of whale
77 fall communities, which are directly linked to the degradation of whale carcasses and on which is
78 based the trophic pyramid at the climax of the ecological succession. Fossil biosignatures such as
79 botryoidal cements, microbial peloids, authigenic pyrite and microborings were found in association
80 with fossil whale bones (Amano and Little, 2005; Kiel, 2008; Shapiro and Spangler, 2009). Similar
81 microbial features were observed also in Upper Cretaceus plesiosaurid bones, suggesting that
82 communities similar to those of whale falls could have existed associated with carcasses of
83 Mesozoic marine reptiles (Kaim et al., 2008). Most of the described bio-sedimentary fabrics are
84 typical of other marine chemosynthetic environments like modern and fossil cold seep deposits,
85 where they are interpreted as microbiologically induced mineralizations (for review see Peckmann
86 and Thiel, 2004; Campbell, 2006; Barbieri and Cavalazzi, 2008). At seeps, consortia of anaerobic
87 methane oxidizing archaea and sulfate reducing bacteria, as a consequence of their metabolism, bio-
88 induce the precipitation of carbonate minerals within the sediments, thus favoring their
89 accumulation as geological deposits. Shapiro and Spangler (2009) suggested that similarly at whale
90 falls botryoidal cements, peloids and framboidal pyrite might precipitate as a consequence of
91 microbial processes during the sulfophilic stage of the ecological succession. To the contrary, Kiel
92 (2008) interpreted similar fabrics (*e.g.*, clotted micrite) from late Eocene-early Oligocene whale
93 falls and the surrounding carbonate concretions, like late diagenetic products formed when the
94 bones were completely buried in sediment, and as a consequence not linked to the sulfophilic stage.
95 In addition, microbial organisms such as algae, bacteria and fungi are known to play an important
96 role in the degradation of apatite bones in marine settings (Jans, 2008). Microborings in fossil whale
97 bones may have thus been originated by one of these trace makers (Amano and Little, 2005; Amano
98 et al., 2007; Kiel, 2008; Shapiro and Spangler, 2009).
99 In their study, Shapiro and Spangler (2009), made a petrographic investigation of fossil
100 whale bones from different depositional settings to verify whether the degree of whale bone

101 degradation is controlled by environmental or depth-related factors. They reported the most
102 convincing evidence of microbial degradation on whale bones from deep water whale falls and the
103 lowest amount and fewest types of degradation on fossil bones from shallow marine depositional
104 environments. Mid to shallow shelf fossil whale bones presented only traces of sulfide crystals and
105 microborings, with no evidence of bacterial peloids and botryoids, the most convincing evidence of
106 a sulfophilic stage according to their interpretation (Shapiro and Spangler, 2009). This result seems
107 to reflect the picture coming from the study of the macro-invertebrate component of both modern
108 and fossil whale falls: unlike their deep water counterpart, natural whale falls are rare on modern
109 shelves, so that the course of the ecological succession is still poorly understood (*see* Smith, 2006).
110 Some knowledge is gained from the fossil record, where chemosymbiotic bivalves associated with
111 whale bones have been once documented in an outer shelf setting (Dominici et al., 2009; Danise et
112 al., 2010). No chemosynthetic activity has been documented so far in shallow shelf and coastal
113 settings. Shallow water whale falls may have played a role in the evolution and dispersal of
114 macrofauna inhabiting modern deep sea chemosynthetic ecosystems. Molecular studies indicate that
115 some specialized deep sea taxa from cold seeps and hydrothermal vents, like mytilid bivalves of
116 subfamily Bathymodiolinae, evolved from shallow water ancestors living on organic falls (Distel et
117 al., 2000; Jones et al., 2006; Duperon, 2010). In fact, despite the antiquity of chemosynthetic
118 ecosystems, molecular clock calibrations infer a Cenozoic origin for most major clades inhabiting
119 modern vents and seeps (Baco et al. 1999; Distel et al. 2000; Kano et al. 2002). Because of the lack
120 of data on macro-invertebrates associated with shallow water whale falls, the study of microbial
121 processes could help in the understanding of whale fall community development on the shelf.
122 In this work we performed a detailed investigation on the fossil bones of a Miocene
123 mysticete whale from shallow water –epineritic– sediments of Northern Italy. We looked for traces
124 of microbial degradation of whale bone lipids with the aim of verifying if the processes described
125 by Shapiro and Splanger (2009) for deep sea whale falls can be extended also to shallower settings

and if the fossil biosignatures observed on the shelf are different from those of the deep sea. In addition to optical microscopy, a combination of analytical techniques, such as scanning electron microscopy, Raman spectroscopy and stable isotope geochemistry were applied for a detailed morphological and geochemical analysis of the studied fossil whale bones. The results allowed us to reconstruct taphonomic and diagentic processes related to the degradation of whale carcasses on the shelf and contribute novel data to the knowledge of the microbial signatures in fossil whale falls.

2. Geological setting

The fossil whale investigated in this paper, hereafter called "*Voghera whale*", was found in the lower member of the Monte Vallassa Formation, part of the Epiligurian succession cropping out in the northernmost part of the Northern Apennines, Italy (Fig. 1). The Monte Vallassa Formation ranges in age from the Serravallian to the Tortonian (13.8-7.2 Ma) and is an approximately 400m thick sequence which registers a transgressive marine cycle spanning from coastal settings to inner and outer shelf deposits (Bellinzona et al., 1971). The lower member is characterized by blue-gray sandy marls rich in macro-invertebrates, like terebratulids among brachiopods, pectinids and ostreids among bivalves, gastropods, isolated corals and echinoids. The sediments are mostly homogenized, with the internal laminations obscured by bioturbation. Locally, hummocky cross stratification structures occur, indicating a storm-dominated shelf environment. Sedimentary data, together with the nature of the rich macrofauna, suggest an epineritic depositional environment, commonly defined as being 0-50m depth (Veronesi, 1997). The lower member is assigned to the Serravallian (13.8-11.6 Ma) based on the occurrence of *Uvigerina barbatula* (Macfad), *Stilotomella verneuili* (D'Orb.), *Orbulina universa* (D'Orb.) and *Globoquadrina dehiscens* (Chap., Parr., Coll.) (Bellinzona et al., 1971).

3. Materials and methods

151 The Voghera whale is curated in the Civico Museo di Scienze Naturali di Voghera (Pavia,
152 Northern Italy). The specimen (V658) was collected in 2007 at Cà del Monte, near to Cecima, Pavia
153 (Fig. 1), and consists of three vertebrae, a few ribs, one scapula and a number of undetermined
154 fragments, enclosed in a carbonate concretion (Fig. 2A-B). The rest of the bones are still *in situ*
155 waiting for further excavations. Fig. 2B shows how the vertebrae are still aligned, suggesting that
156 the bones were subject to little or no reworking. Since a detailed morphological and taxonomical
157 study of the specimen has not been undertaken yet, and is beyond the aims of the present work, it is
158 not possible to provide information about its classification among mysticetes or its estimated body
159 size.
160 Fragmentary bones partially enclosed in the carbonate concretion were selected for the
161 analysis. They were firstly characterized by optical microscopy examination of covered and
162 uncovered standard petrographic thin sections (30 μm thick) and polished surfaces. Optical analyses
163 were performed in transmitted and reflected light using a Zeiss Axioplan2 Imaging microscope
164 equipped with a Zeiss AxioCam digital camera and an Olympus BX51 TH-200 microscope
165 equipped with an Olympus DP12 Digital Microscope Camera. Subsequently, the uncovered thin
166 sections and polished surfaces were examined using a WITec Alpha500 AFM-confocal Raman
167 microscope. Three objectives (Nikon 20x, 50x and 100x) and a frequency doubled Nd:YAG (532
168 nm) Ar-ion 20-mW monochromatic laser source were used to collect the Raman spectra. Beam
169 centering and Raman spectra calibration were performed before spectra acquisition using a Si
170 standard with a characteristic Si Raman peak at 520.4 cm^{-1}. The optimum power for *in situ* analyses
171 of different minerals was experimentally determined between 1.67 and 1.70 nW at the sample
172 surface for the different minerals phases. Raman spectra were recorded and treated using WITec
173 Project 2.00® software, and calibrated after RRUFF-CrystalSleuth DataBase (Laetsch and Downs,
174 2006). Selected portions of the thin sections and freshly broken samples were etched in an aqueous
175 solution of 1% HCl between 5 and 120 seconds, air dried and Au-coated for scanning electron

176 microscope observations and element analysis (SEM-EDX). SEM-EDX imaging and analyses were
177 performed using a Field Emission Gun-SEM (FEG-SEM) Hitachi S4200 and a ZEISS EVO MA 15,
178 both equipped with an X-ray energy dispersive spectrometer system. The operating conditions of
179 the scanning electron microscopes were 5 to 20 keV accelerating voltage for imaging, and 15-20
180 keV for elemental analyses.
181 ^{13}C and ^{18}O stable isotope analyses were performed on carbonate cements inside the whale
182 bones and on the external concretion. Samples (3-5 milligrams) were hand drilled from polished
183 slabs. The powdered samples were dissolved in vacuum in 100% phosphoric acid at 25˚C, and
184 analysed using a Finnigan-MAT 250 mass spectrometer. Reproducibility was checked by replicate
185 analyses (10 identical samples) and the standard deviation was better than ±0.3‰. All results are
186 reported in per mil (‰) deviations from the V-PDB (Vienna-Pee Dee Belemnite) standard.
187 The instruments used are located at the Dipartimento di Scienze della Terra and Centro
188 Interdipartimentale di Microscopia Elettronica e Microanalisi, Università di Firenze (Italy), at the
189 Centre de Biophysique Moléculaire, CNRS, Orléans (France), at the Centre de Microscopie
190 Electronique, Université d'Orléans (France), and at the Stable Isotope Laboratory, Department of
191 Geology, Copenhagen University (Denmark).
192
193 **4. Results**
194 *4.1 Fossil bone preservation*
195 The Voghera whale bones are enclosed in a gray, fine-grained carbonate concretion,
196 consisting of angular siliciclastic grains of quartz, feldspars and micas, and cemented with
197 microcrystalline to small rhombohedral dolomite crystals (maximum size of the main axis 10 μm)
198 (Fig. 3A). Poorly preserved bioclasts of benthic foraminiferal tests and concentrations of fecal
199 pellets close to the fossil bones are also present (Fig. 3B). Fecal pellets are ovoid or elliptical shape,
200 are up to 420 μm in length and contain minor amounts of iron sulfide.

201 The Voghera whale fossil bones are mineralized in carbonate-rich fluorapatite,
202 $Ca_5(PO_4,CO_3)_3F$ (Fig. 4). They preserve both the compact and the cancellous bone tissue (Fig. 5A),
203 are light brown in color in plane polarized and light-black to light-gray in cross polar, exhibiting a
204 birefringence pattern (Figs. 5B,C). Vertebrate compact bones have a relatively solid and dense bone
205 texture, whereas cancellous bones are spongy and highly porous and consist of plates and struts
206 called trabeculae that, in life, are filled with marrow (*sensu* Lyman, 1994). In the Voghera whale,
207 the external part of cancellous bones is highly enriched in dark iron sulfides (Fig. 5A). The original
208 structure of the bones is well preserved: osteons, the major structural elements of bone tissue, and
209 osteocytes, the bone cells, are clearly visible (Figs. 5B-D). As highlighted by the birefringence
210 pattern in cross polars (Fig. 5B), osteons are made by a roughly cylindrical structure of successive
211 concentric lamellae surrounding a centrally located Haversian canal, that in life contains blood
212 vessel and nerves (Lyman, 1994). In the Voghera whale, osteons show a radial system of
213 microcracks (Fig. 5C). Optical microscopy and Raman spectroscopy show reddish, globular
214 aggregates of lepidocrocite, γ-FeO(OH), intimately associated with the tissue of compact and
215 cancellous bones (Fig. 5E). The lepidocrocite grains have a diameter in between 4 and 8 μm,
216 however, rare larger diameter grains up to 40 μm were also observed.
217
218 *4.2 Carbonate cements filling cancellous bones*
219 Cancellous bones are filled with different carbonate phases, which include microcrystalline
220 dolomite, rhombohedral dolomite and euhedral (sparry) calcite (Fig. 6). In thin section,
221 microcrystalline dolomite exhibits a clotted texture, forming dark and cloudy aggregates (Fig. 6A).
222 Locally it forms well organized rounded to sub-rounded peloids with an average radius of 57 μm
223 (min 37.8 μm, max 116 μm) (Figs. 6B-D). Micropeloids show a characteristic internal organization:
224 the inner part consists of a dense aggregate of microcrystalline dolomite, whereas the external
225 portion shows a characteristic rim of rhombohedral dolomite crystals (Fig. 6C). SEM observations

of the micropeloids highlights a dense nucleus of microcrystalline dolomite, 3 to 5 µm in size, and an external rim of rhombohedral dolomite with an average main axis size of 22 µm (Figs 6E). Similar dolomite rhombohedra also line the trabecular bone surface (Fig. 6A,D). Locally, dolomite rhombohedral crystals exhibit a particular habit of small aggregates with a rosette-like form and an average radius of 20 µm (Fig. 7). They can be solitary or coalescent (2-4 bodies), and they are especially common close to bone trabeculae, embedded in the sparry calcite (Fig. 7A). All these rosette-like structures are characterized by a dark, opaque nucleus of a few pyrite framboids surrounded by dolomite rhombohedra (Fig. 7B). Raman analyses performed on the micropeloids and on the rosette-like structures show the presence of disordered carbonaceous matter (DCM) associated with the dolomite crystals and the pyrite framboids, respectively (Fig. 8A-B). Pyrite framboids, commonly associated with the micropeloids and the rosette-like structures, have an average diameter of 6 µm and can be partially or totally oxidized to lepidocrocite (Fig. 8B). SEM-EDX observations show that pyrite framboids can be zoned, with a pyritic internal nucleus (Fe, S) and an external thin rim of lepidocrocite (Fe, O) (Fig. 6F).

4.3 Microborings

Two different microboring morphologies were observed in the Voghera whale samples (Figs 9-11). The first, called Type 1, is the more abundant and occurs both in the inner cancellous bone and in the outer compact bone (Fig. 9). Type 1 microborings have an average diameter of 3.8 µm (observed diameters between 1.7 and 8.4 µm) and their maximum measured length is 37 µm. Optical microscope observations of Type 1 microborings show that they are made by non-bifurcating, slightly curved microtunnels without any preferred orientation (Figs. 9B,D). SEM-EDX analyses show that the wall surface of the microtunnels is intensely encrusted by micron-sized iron-oxides (Figs. 11B-C). On the external part of compact bones Type 1 microborings form a densely tunneled zone which is about 300 µm thick (Figs. 9C-D, 11A). The bioeroded area is delimited by

bright cement lines that mark the boundaries between the secondary osteons of the Haversian systems, whereas the concentric lamellae typical of compact bone osteons are totally obliterated by the intense bioerosion (Figs 9C-D).

Type 2 microborings are less abundant than Type 1 and occur exclusively on the external part of compact bones (Fig. 10). They have an average diameter of 2.3 µm (observed diameter between 1.3 µm and 3.7 µm) and their maximum measured length is 81 µm. They are straight or slightly curved tunnels, often branching with 90° bifurcations (Figs. 10A,D). Some of them exhibit central swellings that can be partially filled by pyrite-lepidocrocite framboids (Fig. 10B). Some filaments reveal internal segmentation (Fig. 10C), and terminal, sack-shaped swellings, 15-20 µm wide, can occur at the tip of some filaments (Fig. 10B). Sometimes microtunnels can be linked to the bone surface by larger apertures (Fig. 10D). Neither Type 1 nor Type 2 microboring development is observed around post-mineralized fractures.

In the same area in which the microborings occur, a 30 µm thick barite coating encrusts the external surface of compact bones (Fig. 11D). SEM-EDX observations indicate that the barite crust has a microcrystalline habit and is associated with a Sr-rich calcite cement (Figs. 11E-F).

4.4 Stable isotope analyses

Carbon and oxygen stable isotope values were obtained from the different carbonate mineral phases within our samples: 1) the dolomite cement of the enclosing concretion, 2) the clotted dolomite and the micropeloids totally or partially occluding voids inside the bones, and 3) the Ca-carbonate, sparry calcite cements found inside and outside the bones (Fig. 12). The dolomite cements of the enclosing concretion have $\delta^{13}C$ values as low as -7.34 ‰ and $\delta^{18}O$ values ranging from +3.86 to +4.36 ‰. The $\delta^{13}C$ and $\delta^{18}O$ values of the microcrystalline dolomite sampled inside bone trabeculae, range from -7.28 to -7.15‰, and from +3.51 to +3.54 ‰ respectively. The sparry

275 calcite occluding voids in- and outside bones has $\delta^{13}C$ values between -1.33 and +0.22‰, with $\delta^{18}O$
276 values ranging between -1.67and -0.3‰.
277
278 **5. Discussion**
279 *5.1 Early stages of bone degradation*
280 The Voghera whale fossil bones are preserved in Ca-rich fluorapatite (Fig. 4), the mineral
281 into which (hydroxyapatite) bones are commonly transformed during diagenesis (Allison and
282 Briggs, 1991). The birefringent pattern of the investigated fossil bones suggests that the bones retain
283 the original alignment of apatite crystals. This pattern is typical of fresh, proteinated bones, despite
284 the loss of the collagen fibers due to fossilization (Hubert et al., 1996). The presence of iron sulfides
285 (pyrite) within the bone matrix may be related to the early stages of bacterial bone decay. Sulfide
286 produced by the bacterial degradation of bone collagen could have induced iron sulfide
287 precipitation inside small void spaces within the bones, such as canaliculi, that are no longer visible
288 because they have been occluded by diagenesis (Pfretzschner, 2001). Similar monosulfide
289 concentrations have also been observed to form layers and infill in the vertebra micropores of
290 modern deep-water whale falls (see Fig. 5 in Allison et al., 1991). In addition, the development of
291 radial microcracks in compact bones could be related to the degradation of collagen during early
292 diagenetic processes as a consequence of the hydration of gelatinized collagen that swelled the
293 bones (Pfretzschner, 2004). Microcracks are considered to enhance the exchange of fluids and
294 chemicals between the bones and the surrounding water during bone decay (Pfretzschner, 2004).
295 The degradation of bone collagen favored the diffusion of oxygen and sulfates from the surrounding
296 water into the Voghera whale bones, which in turn facilitated the onset of decay in the inner part of
297 the bones, where whales host large amounts of lipids. Then, once oxygen was depleted by aerobic
298 heterotrophic bacteria, sulfate reduction and methanogenesis could start (*see* Allison et al., 1991).
299 The concentric zone enriched in iron sulfides observed in the outer part of the Voghera cancellous

300 bones may represent the boundary between an internal region in which sulfate reduction took place
301 at the lipid-water interface and an outer zone where sulfide oxidation and aerobic decay were the
302 dominant processes. A similar distribution of iron sulfides inside whale bones has also been
303 recognized in modern and fossil deep water whale falls (Allison et al., 1991; Shapiro and Spangler,
304 2009).
305
306 *5.3 The origin of microborings*
307 Microborings in the Voghera fossil whale bones were generated prior to the fracturing and
308 mineralization of the bones as they are not concentrated around post-mineralized fractures
309 (Trueman and Martill, 2002). Type 1 microborings are in the same range size of those described in
310 previous studies on deep-water fossil whale-falls (Amano and Little, 2005; Kiel, 2008; Shapiro and
311 Spangler, 2009), plesiosaurid carcasses (Kaim et al., 2008) and in some samples from shallow shelf
312 settings analyzed by Shapiro and Spangler (2009). Type 2 microborings are smaller and similar
313 features have not been described before from fossil whale falls.
314 In previous studies on fossil whale falls, microborings have been assigned to the action of
315 bacteria, algae or fungi, but a more precise determination was not attempted (*e.g.*, Amano and
316 Little, 2005; Kiel, 2008; Shapiro and Spangler, 2009). Although similar microborings have been
317 recognized in modern whale falls (Allison et al., 1991), they have never been studied in detail, and
318 the associated organisms and their metabolism are still unknown. The recent description of the
319 traces left by the bone eating worms *Osedax,* both in modern and fossil whale bones (Higgs et al.,
320 2010; Kiel et al., 2010; Higgs et al., 2011), excludes the possibility that microborings were made by
321 siboglinid worms. *Osedax* traces are one order of magnitude larger than the Voghera whale
322 microborings, and show a very different pattern of destruction of the bones. The morphologies of
323 the studied microborings are similar to the traces left by euendoliths, endolithic microorganisms that
324 actively penetrate into rocks or hard substrates and create microtubular cavities conforming to the

shapes of their bodies (Golubic et al., 1981; McLoughlin et al., 2007). In the marine ecosystem such organisms mainly include phototrophic cyanobacteria and algae and heterotrophic fungi and bacteria, all of which are capable of metabolizing collagen and dissolving the mineral matrix (*e.g.*, Davis, 1997; Trueman and Martill, 2002). While phototrophic euendoliths dominate within the sunlight-illuminated (euphotic) coastal zones in the oceans, the light-independent heterotrophs follow the distribution of organic substrates for food and are found in all depths ranging from shallow coastal waters to the abyssal depths (Golubic et al., 2005 and references therein). As a consequence of convergent evolution of boring and reproductive behavior among unrelated organisms that exploit similar environments in shallow waters, the distinction between the borings of endolithic fungi, filamentous (and sometimes coccoid) cyanobacteria and eukaryotic algae is often difficult (Golubic et al., 2005; Jans, 2008).

The occurrence of the Voghera Type 1 microborings along the internal walls of cancellous bones (Fig. 9A) that is, in an environment not influenced by sunlight, suggests that the responsible organisms are heterotrophic rather than phototrophic. In addition, the absence of bifurcations, the presence of permineralized rims around the borings, and the destructive pattern of the bones support their prokaryotic origin (Turner-Walker, 2008; Turner-Walker et al., 2002; Jans, 2008). Type 2 microborings instead only occur on the external part of the bones (Fig. 10). Here, the presence of dichotomously branched ramifications with internal segmentation and, bag-shaped swellings supports a fungal origin (Schumann et al., 2004; Golubic et al., 2005). According to previous literature on microbial bioerosion of vertebrate fossil bones, Type 1 microborings can be defined as linear longitudinal tunnels and Type 2 microborings as Wedl tunnels (Hacket, 1981; Davis, 1997; Jans, 2008).

5.4 A possible origin of the microcrystalline barite

Microcrystalline barite ($BaSO_4$) was detected on the external surface of the fossil bones (Fig. 11). Barite is known to form in numerous microbially colonized habitats, including marine cold seeps, white smokers, hot springs, and the upper water columns of lakes and oceans (Bonny and Jones, 2008 and references therein). Barite deposits generally form as a result of mixing of soluble barium-containing fluids with sulfate-rich fluids. Deposits formed by direct precipitation from barium-enriched hydrothermal fluids are known as hydrothermal barite. They are restricted to the vicinity of seafloor vents and are commonly associated with anhydrite and sulfides (*e.g.,* Koski et al., 1985). At cold seeps barite precipitation occurs when rising barium-rich fluids derived from the dissolution of biogenic barite deposits react with sulfate-rich, downwards-diffusing seawater or ascending brines (Torres et al., 2003; Aloisi et al., 2004). In the water column, barium sulfate is known to precipitate within microenvironments of decaying planktonic organisms, which may actively or passively accumulate barium and form barite in pelagic sediments underlying high productivity waters (Dehairs et al., 1980; Bishop, 1988; Paytan and Griffith, 2007). Authigenic barite has also been documented in biogenic calcareous rocks where barium is derived from the decomposition of organic matter, plankton and other organisms such as bacteria (Stamatakis and Hein, 1993). Although the morphologies and sizes of marine barite crystals in the water column and in marine sediments indicate a possible biogenic origin, the living organisms which directly precipitate barite have not yet been identified in seawater (González-Munõz et al., 2003). However barite precipitation by living organisms (protozoa) has been observed in lacustrine freshwater environments, where sulfur-metabolizing microbes are able to control and mediate barite saturation (*e.g.,* González-Munõz et al., 2003; Senko et al., 2004). Whale bones can be a good source of barium, thanks to the high concentrations of organic matter, including collagen and lipids. Microcrystalline barite on the external surface of the Voghera fossil whale can have biogenically precipitated around the decaying bones shortly after burial, as in previous reports (Stamatakis and Hein, 1993).

374

375 *5.5 The origin of carbonate cements inside and around the bones*

376 The clotted textures and micropeloidal fabrics in the Voghera fossil whale bones,
377 characterized by richness of dark organic matter, indistinct margins, cloudy interiors, and sulfide
378 minerals (Fig. 6), are similar to those described in a wide variety of different geological settings
379 such as shallow water carbonates and microbialites, coral reef crusts and mud mounds, methane
380 seeps, hot springs and carbonate-rich soils (see Flügel, 2010 for a review). They are the most
381 common microbially induced structures in carbonate rocks and they typically consist of spherical-
382 to-elliptical microscopic aggregates of microcrystalline clots or peloids (*e.g.,* calcite, aragonite),
383 cemented by carbonate and/or sediments (Chafetz, 1986; Burne and Moore, 1987; Shapiro, 2004).
384 The clotted texture is related to small-scale variations in the chemical microenvironment during
385 carbonate precipitation caused by the metabolic activities of microorganisms (Burne and Moore,
386 1987), whereas the peloids are interpreted as microbial bio-products or biominerals that are thought
387 to be precipitated on the surface of bacterial clumps (Chafetz, 1986). Clotted fabrics and
388 micropeloids were recognized also in some of the deep water whale falls investigated by Shapiro
389 and Spangler (2009) and interpreted as biogenic in origin.

390 Our data expand the environmental settings in which similar biosignatures can be found
391 associated with whale bones and clearly confirm that the same model presented by Riding and
392 Tomàs (2006) for the calcification of bacterial micropeloids in Cretaceous stromatolites can also be
393 applicable to fossil whale bones. According to this model the clotted microcrystalline dolomite and
394 the micropeloids of the Voghera whale would represent the products of organic matter decay
395 immediately below the sediment-water interface. During early diagenesis, microbial decay of whale
396 bone lipids induced dolomite precipitation, which in turn induced the calcification of bacterial
397 aggregates forming the nuclei of micropeloids. The spatial distribution of the aggregating bacterial
398 colonies determined the spacing of the micropeloidal masses. When all the lipids were consumed

399 and the peloids overgrew, the sparry calcite cement occluded the water-filled voids. The peculiar
400 architecture of rosette-like structures in Fig. 7 (spheroidal dolomitic body generated around an
401 opaque nucleus of few pyrite framboids) is reminiscent of small peloids, although they lack the
402 inner filling of microcrystalline dolomite. They could also represent bacterially induced precipitates
403 overgrown by single euhedral dolomite crystals instead of being completely lithified by
404 microcrystalline dolomite, as supposed for similar dolomite aggregates from a Miocene methane
405 seep of northern Italy (Cavagna et al., 1999).

406 A biogenic origin of the rosette-like structures and the micropeloids as well is further
407 supported by the presence of disordered carbonaceous matter as detected by Raman microscopy.
408 The first order G (~1350 cm^{-1}) and D (~1360 cm^{-1}) bands of carbonaceous matter were observed in
409 close association with both of them (Fig. 8). G and D bands of the Raman spectra represent a
410 mixture of crystalline (G: graphite) and poorly organized (D: disordered) carbonaceous material,
411 respectively (*e.g.,* Jehlička and Bény, 1992; Pasteris and Wopenka, 2003). The Raman analytical
412 technique, recently introduced to paleontology (*e.g.,* Kudryavtsev et al., 2001), is widely used for
413 the *in situ* identification of minerals and their molecular-structural study, and to document the
414 molecular structure and geochemical maturity of organic carbonaceous matter, *e.g.* graphite and
415 graphite-like carbonaceous mineraloids (Jehlička and Bény, 1992; Pasteris and Wopenka, 2003;
416 Marshall et al., 2010). Although the presence of disordered carbonaceous matter in association with
417 the Voghera whale micropeloids and the rosette-like structures alone is not an unequivocal proof of
418 their biologic origin, it represents a further clue supporting their biogenicity if put together with all
419 the other evidences discussed (biosignature suite *sensu* Boston et al., 2001)

420 The precipitation of dolomite in the micropeloids of the Voghera fossil whale bones was
421 probably determined by the local chemistry of the pore waters. Dolomite precipitation, in fact, is
422 known to be inhibited by normal marine sulfate concentration, whereas it is favored when sulfates
423 are removed from the pore waters by an intense reducing bacterial activity (Kastner, 1984). In

424 particular, the degradation of organic matter by sulfate reducing bacteria can promote early
425 dolomite precipitation by simultaneously increasing the carbonate alkalinity and reducing near zero
426 the sulfate ion concentration (Compton, 1988). The sediment depth of early dolomite precipitation
427 depends on the organic input, the rate of sulfate reduction and sedimentation rate, and can begin at
428 less than 1m below the sediment sea-water interface (Mazzullo, 2000). An intense sulfate reduction
429 is furthermore suggested by the common co-occurrence in the Voghera samples of pyrite framboids
430 associated with the dolomitic clots and the rhombohedric dolomite cements. Microbially produced
431 pyrite framboids and crystals are common in sedimentary rocks, especially in fine-grained
432 lithologies (*e.g.*, Berner, 1970). However the association of framboidal pyrite with authigenic
433 carbonates is less common, and in seep-related authigenic carbonates it is considered to be a
434 paleoenvironmental indicator for bacteria sulfate reduction independent of burial diagenesis
435 (Cavagna et al., 1999; Shapiro, 2004; Cavalazzi et al., 2011).

436 The presence of iron oxide-hydroxides (lepidocrocite) associated with iron sulfides suggests
437 a partial oxidative diagenetic transformation of the original pyrite (Bailey et al., 2010; Cavalazzi et
438 al, 2011). Iron oxides and oxide-hydroxides are common in fossil bones (Wings, 2004) and they can
439 originate during late diagenetic processes when external oxidants enter the fossil bones and
440 transform the existing minerals (Pfretzschner, 2001). Pyrite framboids surrounded by a thin rim of
441 lepidocrocite, as those observed at Voghera, resemble the structures described from a Pleistocene
442 methane seep in California where iron oxides and oxide-hydroxides (*e.g.*, hematite, goethite) in
443 association with authigenic sulfides precipitated as a consequence of the anaerobic oxidation of
444 methane and bacterial sulfate reduction (Bailey et al., 2010). Here the diagenetic oxidation of
445 reduced minerals was interpreted as the transition from sulfidic, anoxic conditions, to well-
446 oxygenated conditions after the cessation of the seep activity (Bailey et al., 2010). Similarly the
447 oxidation of the pyrite framboids of the Voghera whale may have occurred during the late

448 diagenetic history of the bones once the whale bone lipids were consumed and sulfate reduction
449 processes ceased.
450
451 *5.6 Carbon and oxygen stable isotope signatures*
452 Carbonate minerals derived from the microbial oxidation of organic matter are characterized
453 by distinctive carbon and oxygen stable isotope signatures which can help the understanding of the
454 processes involved in their precipitation. In particular, sedimentary organic carbon is depleted in
455 ^{13}C (~- 25%) relative to seawater ($\delta^{13}C \sim 0\%$), and carbonate derived from degradation of organic
456 matter inherits the carbon isotope composition of its precursor (Coleman et al., 1993). The oxygen
457 isotopic composition is thought to be mainly determined by the temperature of carbonate
458 precipitation, ^{18}O-enriched isotopic composition can be related to low bottom water temperatures in
459 marine shelf environments, whereas more ^{18}O-depleted values are most likely the result of
460 continued precipitation at higher temperatures associated with greater burial depth (Mozley and
461 Burns, 1993).
462 The depleted $\delta^{13}C$ values of the Voghera whale microcrystalline dolomite sampled inside
463 bone trabeculae, as low as -7.28‰, suggest that the dolomite precipitation was driven by sulfate
464 reduction processes during the bacterial oxidation of organic matter. However, the difference
465 compared to theoretical values implies the mixing with a carbonate source of marine origin
466 (Raiswell and Fisher, 2000). The measured values of $\delta^{13}C$ could have also been affected by
467 sampling methods. Because microcrystalline dolomite and sparry calcite occur on very small spatial
468 scale, their sampling with a hand held micro-drill could have caused contamination between
469 neighboring carbonate phases. As a consequence, it could have produced more enriched $\delta^{13}C$ values
470 for the microcrystalline dolomite. The similar carbon and oxygen isotopic signal obtained both for
471 the dolomite intimately associated with cancellous bones and for the dolomite in the enclosing
472 concretion suggests that they precipitated in similar geochemical conditions. The slightly high $\delta^{18}O$

473 values for the dolomite cements inside and outside the bones are indicative of low bottom water
474 temperatures on the shelf and low late-diagenetic alteration (Mozley and Burns, 1993). Finally the
475 carbon and oxygen stable isotope values of the sparry calcite cement inside and outside the bones
476 (avg $\delta^{13}C$: -0.55 ‰; avg $\delta^{18}O$: -0.98 ‰) are consistent with a (late) precipitation in chemical
477 equilibrium with seawater (Mozley and Burns, 1993). Isotope data of the two main carbonate
478 phases, together with their spatial distribution, structures and mineralogy described and previously
479 discussed, are consistent with the hypothesis that dolomite cements are of microbial origin and
480 precipitated early during the sediment's story. To the contrary sparry calcite originated during late
481 diagenetic processes. As observed by Kiel (2008), who analyzed enclosing concretions and cements
482 from inside the bones of late Eocene-early Oligocene deep water whale-falls of the Lincoln Creek
483 Formation (Washington State, USA), the carbonate concretion formed after that the bones were
484 buried in the sediments.
485
486 *5.7 Taphonomic model: a hypothesis*
487 All the collected data interpreted following previous studies on modern and fossil whale
488 falls and on similar reduced environments like methane seeps, allow us to reconstruct the possible
489 taphonomic history of the Voghera fossil whale. Although shark teeth were not found associated
490 with the fossil bones, which would be a direct clue for scavenging, we assume that once the carcass
491 arrived to the sea floor soft, fleshy tissues were rapidly removed by mobile scavengers to prevent
492 the carcass refloating after production of decay gasses. In fact, in contrast to deep sea settings where
493 hydrostatic pressure limits the generation of buoyant decompositional gases, at shallow depths (<
494 1000 m) gas generation will tend to refloat whale carcasses unless gas generation is hindered (see
495 Schäfer, 1972; Allison et al., 1991). The decay of the bone organic matter started with the bacterial
496 degradation of bone collagen, as testified by the precipitation of iron sulfides in the bone matrix and
497 by radial micro-cracks in compact bones. Saprophagous bone borers, probably feeding on bone

collagen, created microscopic tunnels in the external surface of the bones, migrating progressively inward. All these processes enhanced the inflow of seawater inside the bones, allowing the diffusion of sulfate. After the consumption of free oxygen by aerobic heterotrophic bacteria, the decay of bone lipids in the marrow cavities of cancellous bones was facilitated by anaerobic sulfate reduction. Microbial sulfide production induced the precipitation of iron sulfides in the external area of trabecular bones. Notwithstanding the occurrence of iron sulfides suggests the presence of elevated H_2S concentrations within the whale bones, no macrofauna indicative of the onset of a sulfophilic stage of the ecological succession, nor fossil traces of sulfur oxidizing bacteria, were found associated with the Voghera whale. It is hypothesized that the carcass was buried before all the whale bone lipids were consumed, and that sulfate reduction processes promoted the precipitation of microcrystalline- and euhedral-dolomite cements both inside bone trabeculae and in nearby sediments. A carbonate concretion formed around the whale bones. Whale organic matter decay favored the contemporaneous accumulation of barium and the consequent precipitation of microcrystalline barite on the surface of the bones. When all bone lipids were consumed, microbial dolomite precipitation ceased and sparry calcite precipitation in equilibrium with sea water occluded the remaining voids of trabecular bones. Finally, during late diagenetic processes, external oxidants induced the partial oxidation of pyrite into iron oxide-hydroxides. It is difficult to estimate how long the carcass remained on the sea floor before burial. In an epineritic, storm-dominated environment like the lower member of the Monte Vallassa formation, a single storm event may have sufficed to bury the carcass. The study of lower Jurassic ammoniteferous concretions with microbial fabrics and cements similar to those observed at Voghera, indicates that instantaneous depositional events favor the onset of early diagenetic processes and the associated intense microbial activity (Curtis et al., 2000).

6. Conclusions

523 The detailed microfacies and geochemical analyses of Miocene fossil whale bones
524 (Serravallian, Voghera, northern Italy) allowed us to reconstruct the main thaphonomic and
525 diagenetic events related to the decay of a whale carcass in a shallow water, epineritic environment.
526 Multiple evidences of microbial processes linked to the carcass degradation were detected, related
527 to both pre- and post-burial phases.
528 The analysis of microborings allowed us to restrict the range of possible trace makers. In
529 particular, traces were left by two different types of euendolith microorganisms, a prokaryote and a
530 fungus. They probably fed on the whale bone collagen, and participated to the decay of the bones
531 when they were still exposed on the sea floor. Future analyses on similar organisms living at
532 modern whale falls may help a better understanding of their metabolism and trophic role.
533 Evidence of pre-burial sulfate reduction processes and hydrogen sulfide emission around the
534 bones is scanty and no decisive. The most convincing evidence is the presence of a concentric zone
535 enriched in iron sulfides in the outer part of cancellous bones, representing the boundary between an
536 internal region of sulfate reduction at the lipid-water interface and an outer zone of sulfide
537 oxidation. These structures are also observed in modern whale falls. All the other microbially-
538 mediated biofabric and biominerals observed in the bones and in the enclosing concretion testify for
539 post-burial anaerobic decay of bone lipids by sulfate reduction. Microbial peloids, rosette-like
540 structures, clotted textures and microcrystalline barite formed during early diagenetic processes.
541 Iron sulfides are thus the only evidence of the possible onset of a sulfophilic stage of the ecological
542 succession before the bones were buried below sediments. The occurrence of clotted textures and
543 micropeloids associated with whale bones cannot be used alone as a fossil evidence of the
544 development of a whale fall sulfophilic stage. The same fabrics can in fact form after and in the
545 absence of a whale fall community as currently understood.

546 The present conclusions confirm that the occurrence of the hard parts of chemosynthetic
547 invertebrates associated with fossil whale bones is still the more convincing evidence of the
548 development of a sulfide-base chemoautotrophic ecosystem.
549
550 **Acknowledgements**
551 The authors thank Birger Schmitz for the isotope analyses, Annie Richard and Maurizio
552 Ulivi for their assistance during SEM-EDS analyses, Nicola Cipriani and Marta Marcucci for their
553 help in petrographic and micropaleontological analyses, respectively. We thank Crispin T.S. Little
554 for suggestions on the first draft of the manuscript and Richard Twitchett for his helpful comments
555 on the final version. We also thank Steffen Kiel and an anonymous reviewer for their help in
556 improving the manuscript. This work was supported by MIUR-PRIN grant 2007 (SM). BC and FW
557 would like to thank LeStudium, Centre for Advanced Research, Orléans, France.
558
559
560 **References**
561 Allison, P.A., Briggs, D.E.G., 1991. The taphonomy of soft-bodied animals, in: Donovan, S.K.
562 (Ed.), Fossilization: the process of taphonomy. Belhaven Press, London, pp. 120–140.
563 Allison, P.A., Smith, C.R., Kukert, H., Deming, J.W., Bennett, B.A., 1991. Deep-water
564 taphonomy of vertebrate carcasses: a whale skeleton in the bathyal Santa Catalina Basin.
565 Paleobiology 17, 78–89.
566 Aloisi, G., Wallmann, K., Bollwerk, S.M., Derkachev, A., Bohrmann, G., Suess, E., 2004. The
567 effect of dissolved barium on biogeochemical processes at cold seeps. Geochimica et
568 Cosmochimica Acta 68, 1735–1748.
569 Amano, K., Little, C.T.S., 2005. Miocene whale-fall community from Hokkaido, northern
570 Japan. Palaeogeography, Palaeoclimatology, Palaeoecology 215, 345–356.

571 Amano, K., Little, C.T.S., Inoue, K., 2007. A new Miocene whale-fall community from Japan.
572 Palaeogeography, Palaeoclimatology, Palaeoecology 247, 236–242.
573 Baco, A.R., Smith, C.R., Peek, A.S., Roderick, G.K., Vrijenhoek, R.C., 1999. The phylogenetic
574 relationships of whalefall vesicomyid clams based on mitochondrial COI DNA sequences. Marine
575 Ecology Progress Series 182:137–147.
576 Bailey, J.V., Raub, T.D., Meckler, A.N., Harrison, B.K., Raub, T.M.D., Green, A.M., Orphan,
577 V.J., 2010. Pseudofossils in relict methane seep carbonates resemble endemic microbial consortia.
578 Palaeogeography, Palaeoclimatology, Palaeoecology 285, 131–142.
579 Barbieri, R., Cavalazzi, B., 2008. Fossil microorganisms at methane seeps: an astrobiological
580 perspective, in: Seckbach, J., Walsh, M. (Eds.), From Fossils to Astrobiology. Records of Life on
581 Earth and the search for Extraterrestrial Biosignatures Series: Cellular Origin, Life in Extreme
582 Habitats and Astrobiology. Springer-Verlag, pp. 297–318.
583 Bellinzona, G., Boni, A., Braga, G., Marchetti, G., 1971. Note illustrative della Carta Geologica
584 d'Italia in scala 1:100.000, Foglio 71, Voghera. Servizio Geologico d'Italia, Roma, pp. 121.
585 Bennett, B.A., Smith, C.R., Glaser, B., Maybaum, H.L., 1994. Faunal community structure of a
586 chemoautotrophic assemblage on whale bones in the deep northeast Pacific Ocean. Marine Ecology
587 Progress Series 108, 205–223.
588 Berner, R.A., 1970. Sedimentary pyrite formation. American Journal of Science 268, 1–23.
589 Bishop, J.K.B., 1988. The barite-opal-organic carbon association in oceanic particulate matter.
590 Nature 332, 341–343.
591 Bonny S.M., Jones, B., 2008. Experimental precipitation of barite ($BaSO_4$) among streamers of
592 sulfur-oxidizing bacteria. Journal of Sedimentary Research 78, 357–365.
593 Boston, P.J., Spilde, M.N., Northup, D.E., Melim, L.A., Soroka, D.A., Kleina, L.G., Lavoie,
594 K.H., Hose, L.D., Mallory, L.M., Dahm, C.N., Crossey, L.J., Scheble, R.T., 2001. Cave
595 biosignature suites: Microbes, minerals and Mars. Astrobiology 1, 25–55.

596 Burne, R.V., Moore, L.S., 1987. Microbialites: organosedimentary deposits of benthic microbial
597 communities. Palaios 2, 241–254.
598 Campbell, K.A., 2006. Hydrocarbon seep and hydrothermal vent paleoenvironments: past
599 developments and future research directions. Palaeogeography, Palaeoclimatology, Palaeoecology
600 232, 362–407.
601 Cavagna, S., Clari, P., Martire, L., 1999. The role of bacteria in the formation of cold seep
602 carbonates: geological evidence from Monferrato (Tertiary NW Italy). Sedimentary Geology 126,
603 253–270.
604 Cavalazzi, B., Barbieri, R., Cady, S.L., George, A.D., Gennaro, S., Westall, F., Lui, A., Canteri,
605 R., Rossi, A.P., Ori, G.G., Taj-Eddine, K., 2011. Iron-rich framboids from a hydrocarbon-related
606 Devonian mound (Anti-Atlas, Morocco) as pseudofossils of fossil bacterial colonies. Sedimentary
607 Geology, doi:10.1016/j.sedgeo.2011.09.007
608 Chafetz, H.S., 1986. Marine peloids; a product of bacterially induced precipitation of calcite.
609 Journal of Sedimentary Research 56, 812–817.
610 Clari, P., Dela Pierre F., Martire L., Cavagna S., 2009. The Cenozoic CH4-derived carbonates of
611 Monferrato (NW Italy): A solid evidence of fluid circulation in the sedimentary column. Marine
612 Geology 265, 167-184.
613 Coleman, M.L., Raiswell, R., Brown, A., Curtis, C.D., Aplin, A.C., Ortoleva, P.J.,
614 Gruszczynski, M., Lyons, T., Lovley, D.R., Eglinton, G., 1993. Microbial mineralization of organic
615 matter: mechanisms of self-organization and inferred rates of precipitation of diagenetic minerals.
616 Philosophical Transactions: Physical Sciences and Engineering 344, 69–87.
617 Compton, J.S., 1988. Degree of supersaturation and precipitation of organogenic dolomite.
618 Geology 16, 318–321.
619 Curtis, C.D., Cope, J.C.W., Plant, D., Macquaker, J.H.S., 2000. ‘Instantaneous’ sedimentation,
620 early microbial sediment strengthening and a lengthy record of chemical diagenesis preserved in

621 Lower Jurassic ammonitiferous concretions from Dorset. Journal of the Geological Society 157,
622 165–172.
623 Danise, S., Dominici, S., Betocchi, U., 2010. Mollusk species at a Pliocene shelf whale fall
624 (Orciano Pisano, Tuscany). Palaios 25, 449–556.
625 Davis, P.G., 1997. The bioerosion of bird bones, International Journal of Osteoarchaeology 7,
626 388–401.
627 Dehairs, F., Chesselet, R., Jedwab, J., 1980. Discrete suspended particles of barite and the
628 barium cycle in the open Ocean. Earth and Planetary Science Letters 49, 528–550.
629 Deming, J.W., Reysenbach, A.L., Macko, S.A., Smith, C.R., 1997. Evidence for the microbial
630 basis of a chemoautotrophic invertebrate community at a whale fall on the deep seafloor: bone-
631 colonizing bacteria and invertebrate endosymbionts. Microscopy Research and Technique 37, 162–
632 170.
633 Distel, D.L., Baco, A.R., Chuang, E., Morrill, W., Cavanough, C., Smith, C.R., 2000. Do
634 mussels take wooden steps to deep-sea vents? Nature 403, 725–726.
635 Dominici, S., Cioppi, E., Danise, S., Betocchi, U., Gallai, G., Tangocci, F., Valleri, G., Monechi,
636 S., 2009. Mediterranean fossil whale falls and the adaptation of mollusks to extreme habitats.
637 Geology 37, 815–818.
638 Dubilier, N., Bergin, C., Lott, C., 2008. Symbiotic diversity in marine animals: the art of
639 harnessing chemosynthesis. Nature Reviews 6, 725–740.
640 Duperon, S., 2010. The diversity of deep-sea mussels and their bacterial symbioses, in: Kiel S.
641 (Ed.), The Vent and Seep Biota: Aspects from Microbes to Ecosystems. Springer, pp. 137–168.
642 Flügel, E., 2010. Microfacies of carbonate rocks, second ed. Springer, Berlin.
643 Goedert, J.L., Squires, R.L., Barnes, L.G., 1995. Paleoecology of whale-fall habitats from deep-
644 water Oligocene rocks, Olympic Peninsula, Washington state. Palaeogeography, Palaeoclimatology,
645 Palaeoecology 118, 151–158.

646 Goffredi, S.K., Paull, C.K., Fulton-Bennett, K., Hurtado L.A., Vrijenhoek, R.C., 2004. Unusual
647 benthic fauna associated with a whale fall in Monterey Canyon, California. Deep-Sea Research I
648 51, 1295–1306.
649 Goffredi, S.K., Wilpiszeski, R., Lee, R., Orphan, V.J., 2008. Temporal evolution of methane
650 cycling and phylogenetic diversity of archaea in sediments from a deep-sea whale-fall in Monterey
651 Canyon, California. The International Society for Microbial Ecology Journal 2, 204–220.
652 Golubic, S., Friedmann, I., Schneider, J., 1981. The lithobiontic ecological niche, with special
653 reference to microorganisms. Journal of Sedimentary Petrology 51, 475–478.
654 Golubic, S., Radtke, G., Le Campion-Alsumard,T., 2005. Endolithic fungi in marine
655 ecosystems. Trends in Microbiology 13, 229–235.
656 Gonzaléz-Munoz, M.T., Fernández-Luque, B., Martínez-Ruiz, F., Chekroun, K.B., Arias, J.M.,
657 Rodríguez-Gallego, M., Martínez-Canamero, M., De Linares, C., Paytan, A., 2003. Precipitation of
658 Barite by *Myxococcus xanthus*: Possible implications for the biogeochemical cycle of Barium.
659 Applied and Environmental Microbiology 69, 5722–5725.
660 Hachiya, K., 1992. A unique community in the reduced environment found from the Morozaki
661 Group. Kaseki no Tomo (Pubblication of the Tokai Fossil Society) 39, 37–41.
662 Hackett, C.J., 1981. Microscopical focal destruction (tunnels) in exhumed human bones.
663 Medicine, Science and the Law, 21: 243–265.
664 Higgs, N.D., Glover, A.G., Dahlgren, T.G., Little, C.T.S., 2010. Using computed-tomography to
665 document borings by *Osedax mucofloris* in whale bone. Cahiers de Marine Biologie 51, 401–405.
666 Higgs, N.D., Little, C.T.S., Glover, A.G., Dahlgren, T.G., Smith, C.R., Dominici S., 2011.
667 Evidence of *Osedax* worm borings in Pliocene (~3 Ma) whale bone from the Mediterranean.
668 Historical Biology, DOI:10.1080/08912963.2011.621167.

669 Hubert, J.F., Panish, P.T., Prostak, K.S., Chure, D.J., 1996. Chemistry, microstructure,
670 petrology, and diagenetic model of Jurassic dinosaur bones, Dinosaur National Monument, Utah.
671 Journal of Sedimentary Research 66, 531–547.
672 Jans, M.M.E., 2008. Microbial bioerosion of bone – a review, in: Wisshak, M., Tapanila L.
673 (Eds.), Current development in Bioerosion. Erlangen Earth Conference Series, pp. 397–413.
674 Jehlička, J., Bény, C., 1992. Application of Raman microspectrometry in the study of structural
675 changes in Precambrian kerogens during regional metamorphism. Organic Geochemistry 18, 211–
676 213.
677 Jones, W.J., Won, Y.J., Maas, P.A.Y., Smith, P.J., Lutz, R.A., Vrijenhoek, C., 2006. Evolution
678 of habitat use by deep-sea mussels. Marine Biology 148, 841–851.
679 Kaim, A., Kobayashi, Y., Echizenya, H., Jenkins, R.G., Tanabe, K., 2008. Chemosynthesis
680 based associations on Cretaceous plesiosaurid carcasses. Acta Palaeontologica Polonica 53, 97–104.
681 Kano, Y., Chiba, S., Kase, T., 2002. Major adaptive radiation in neritopsine gastropods
682 estimated from 28S rRNA sequences and fossil records. Proceedings of the Royal Society of
683 London B 269:2457–2465.
684 Kastner, M., 1984. Control of dolomite formation. Nature 311, 410–411.
685 Kiel, S., 2008. Fossil evidence for micro- and macrofaunal utilization of large nektonfalls:
686 examples from early Cenozoic deep-water sediments in Washington State, USA. Palaeogeography,
687 Palaeoclimatology, Palaeoecology 267, 161–174.
688 Kiel, S., Goedert, J.L., 2006. Deep-sea food bonanzas: early Cenozoic whale-fall communities
689 resemble wood-fall rather than seep communities. Proceedings of the Royal Society of London B
690 273, 2625–2631.
691 Kiel, S., Little C.T.S., 2006. Cold-seep mollusks are older than the general marine mollusk
692 fauna. Science 313, 1429-1431.

693 Kiel, S., Goedert, J.L., Kahl, W-A., Rouse, G.W., 2010. Fossil traces of the bone-eating worm
694 *Osedax* in early Oligocene whale bones. Proceedings of the National Academy of Science, USA
695 107, 8656–8659.
696 Koski, R.A., Lonsdale, P.F., Shanks, W.C., Vemdt, M.E., Howe, S.S., 1985. Mineralogy and
697 geochemistry of a sediment hosted hydrothermal sulfide deposits from the southern trough of the
698 Guaymas Basin, Gulf of California. Journal of Geophysical Research 90, 6695–6707.
699 Kudryavtsev, A.B., Schopf, J.W., Agresti, D.G., Wdowiak, T J., 2001. In situ laser-Raman
700 imagery of Precambrian microscopic fossils. Proceedings of the National Academy of Sciences
701 USA 98, 823–826.
702 Laetsch, T.A., Downs, R.T., 2006. Software for identification and refinement of cell parameters
703 from powder diffraction data of minerals using the RRUFF Project and American Mineralogist
704 Crystal Structure Databases. Program and Abstracts of the 19th General Meeting of the
705 International Mineralogical Association in Kobe, Japan. P08-25.
706 Lyman, R.L., 1994. Vertebrate taphonomy. Cambridge University Press, Cambridge.
707 Marshall, C.P., Edwards, H.G.M., Jehlicka, J., 2010. Understanding the application of Raman
708 spectroscopy to the detection of traces of life. Astrobiology 10, 229–243.
709 Mazzullo, S.J., 2000. Organogenic dolomitization in peritidal to deep-sea sediments. Journal of
710 Sedimentary Research 70, 10–23.
711 McLoughlin, N., Brasier, M.D., Wacey, D., Green, O.R., Perry, R.S., 2007. On Biogenicity
712 Criteria for Endolithic Microborings on Early Earth and Beyond. Astrobiology 7, 10–26.
713 Mozley, P.S, Buns S.J, 1993. Oxygen and carbon isotopic composition of marine carbonate
714 concretions: an overview. Journal of Sedimentary Petrology 63, 73–83.
715 Naganuma, T., Wada, H., Fujioka, K., 1996. Biological community and sediment fatty acids
716 associated with the deep-sea whale skeleton at the Torishima Seamount. Journal of Oceanography
717 52, 1–15.

718 Nesbitt, E.A., 2005. A novel trophic relationship between cassid gastropods and mysticete
719 whale carcasses. Lethaia 38, 17–25.
720 Pasteris, J.D., Wopenka, B., 2003. Necessary, but not sufficient: Raman identification of
721 disordered carbon as a signature of ancient life. Astrobiology 3, 727–738.
722 Paytan, A., Griffith, E.M., 2007. Marine barite: Recorder of variations in ocean export
723 productivity. Deep-Sea Research II 54, 687–705.
724 Peckmann, J., Thiel, V., 2004. Carbon cycling at ancient methane-seeps. Chemical Geology
725 205, 443–467.
726 Pfretzschner, H.U., 2001. Pyrite in fossil bone. Neues Jahrbuch für Geologie und Paläontologie
727 Abhandlungen 220, 1–23.
728 Pfretzschner, H.U., 2004. Fossilization of Haversian bone in aquatic environments. Comptes
729 Rendus Palevol 3, 605–616.
730 Pyenson, N.D., Haasl, D.M., 2007. Miocene whale-fall from California demonstrates that
731 cetacean size did not determine the evolution of modern whale-fall communities. Biology Letters
732 (Palaeontology) 3, 709–711.
733 Raiswell, R., Fisher, Q.J., 2000. Mudrock-hosted carbonate concretions: a review of growth
734 mechanisms and their influence on chemical and isotopic compostion. Journal of the Geological
735 Society, London 157, 239–251.
736 Riding, R., Tomás, S., 2006. Stromatolite reef crusts, Early Cretaceous, Spain; bacterial origin
737 of in situ-precipitated peloid microspar? Sedimentology 53, 23–34.
738 Schäfer, W., 1972. Ecology and palaeoecology of marine environments. Chicago, University of
739 Chicago Press.
740 Schumann, G., Manz, W., Reitner, J., Lustrino, M., 2004. Ancient fungal life in North Pacific
741 Eocene oceanic crust. Geomicrobiology Journal 21, 241–246.

742 Senko, J.M., Campbell, B.S., Henriksen, J.R., Elshahed, M.S., Dewers, T.A., Krumholz, L.R.,
743 2004. Barite deposition resulting from phototrophic sulfide-oxidizing bacterial activity. Geochimica
744 et Cosmochimica Acta 68, 773–780.
745 Shapiro, R.S., 2004. Recognition of Fossil Prokaryotes in Cretaceous Methane Seep Carbonates:
746 Relevance to Astrobiology. Astrobiology 4, 438–449.
747 Shapiro, R.S., Spangler, E., 2009. Bacterial fossil record in whale-falls: Petrographic evidence
748 of microbial sulfate reduction. Palaeogeography, Palaeoclimatology, Palaeoecology 274, 196–203.
749 Smith, C.R., 2006. Bigger is better: the role of whales as detritus in marine ecosystems, in:
750 Estes, J.A., De Master, D.P., Brownell Jr., R.L., Doak, D.F., Williams, T.M. (Eds.), Whales,
751 Whaling and Ocean Ecosystems. University of California Press, Berkeley, CA, USA, pp. 286–301.
752 Smith, C.R., Baco, A.R., 2003. Ecology of whale falls at the deep-sea floor. Oceanography and
753 Marine Biology: an Annual Review 41, 311–354.
754 Smith, C.R., Maybaum, H.L., Baco, A.R., Pope, R.H., Carpenter, S.D., Yager, P.L., Macko,
755 S.A., Deming, J.W., 1998. Sediment community structure around a whale skeleton in the deep
756 Northeast Pacific: macrofaunal, microbial and bioturbation effects. Deep-Sea Research II 45, 335–
757 364.
758 Squires R.L., Goedert J.L., Barnes L.G., 1991. Whale carcasses. Nature 349, 574.
759 Stamatakis M.G., Hein J.R., 1993. Origin of barite in tertiary marine sedimentary rocks from
760 Lefkas Island, Greece. Economic Geology 88, 91–103.
761 Torres, M.E., Bohrmann, G., Dubé, T.E., Poole, F.G., 2003. Formation of modern and Paleozoic
762 stratiform barite at cold methane seeps on continental margins. Geology 31, 897–900.
763 Treude, T., Smith, C.R., Wenzhöfer, F., Carney, E., Bernardino, A.F., Hannides, A.K., Krüger,
764 M., Boetius, A., 2009. Biogeochemistry of a deep-sea whale fall: sulphate reduction, sulfide efflux
765 and methanogenesis. Marine Ecology Progress Series 382, 1–21.

766 Trueman, C.N., Martill, D.M., 2002. The long-term survival of bone: the role of bioerosion.
767 Archaeometry 44, 371–382.
768 Turner-Walker, G., 2008. The chemical and microbial degradation of bones and teeth, in:
769 Pinhasi, R., Mays, S. (Eds.), Advances in human paleopathology. Wiley & Sons, Chichester, pp. 1–
770 29.
771 Turner-Walker, G., Nielsen-Marsh, C.M., Syversen, U., Kars, H., Collins, M.J., 2002. Sub-
772 micron spongiform porosity is the major ultra-structural alteration occurring in archaeological bone.
773 International Journal of Osteoarchaeology 12, 407–414.
774 Veronesi, M., 1997. Analisi sedimentoloigico-stratigrafica sulle Arenarie di M. Vallassa e sulle
775 Arenarie di Serravalle tra Pietravigna (PV) e Gavi (AL). Master thesis, Università degli Studi di
776 Pavia, pp. 139.
777 Wings, O., 2004. Authigenic minerals in fossil bones from the Mesozoic of England: poor
778 correlation with depositional environments. Palaeogeography, Palaeoclimatology, Palaeoecology,
779 204: 15–32.
780

781 **FIGURE CAPTIONS**

782

783 **Fig. 1.** Schematic geological map of the Voghera whale site, Northern Italy. The Voghera whale
784 was recovered within middle Miocene blue-grey sandy marls belonging to the Epiligurid Monte
785 Vallassa Formation (arrow). Oblique lines: areas of outcrop of Alpine units; horizontal lines: areas
786 of outcrop of Apennine units; light-grey: Oligo–Miocene sedimentary successions of Monferrato,
787 Torino Hill and Tertiary Piedmont Basin; dark-grey: Epiligurids; unpatterned: Plio–Pleistocene
788 sediments. Figure modified from Clari et al., 2009.

789

790

791 **Fig. 2. The** Voghera whale, specimen V658, Civico Museo di Scienze Naturali di Voghera (Italy).
792 The fossil whale bones, vertebrae and ribs, are enclosed in a carbonate concretion **A.** Upper view of
793 the main block enclosing the bones. **B.** Lower view of the same block. Note the alignment of the
794 two vertebrae. wb: whale bone; ec: enclosing concretion.

795

796

797 **Fig. 3.** Transmitted light photomicrographs of petrographic thin sections of the Voghera whale
798 bones and the enclosing carbonate concretion. **A.** Fossil whale bone (wb) and the enclosing
799 concretion (ec). The enclosing concretion consists of a siliciclastic matrix cemented by
800 microcrystalline dolomite. Note the canals of compact bones (wb) filled by sparry calcite (sc). **B.**
801 Enclosing concretion with fecal pellets (arrows).

802

803

804 **Fig. 4.** Raman spectrum of the Voghera whale fossil bones. The bones are preserved as Ca-rich
805 fluoroapatite, $Ca_5(PO_4,CO_3)_3F$.

Fig. 5. Transmitted light photomicrographs of petrographic thin sections of the Voghera whale bones. **A.** Bone structure with well preserved compact and cancellous bone tissue. Note black iron mono sulfides especially concentrated at the compact-cancellous bone interface (arrows). **B.** Detail of compact bone as observed in cross polarized light. The birefringent pattern of the osteons emphasizes the concentric lamellar structures (arrow) surrounding the central Haversian canal. **C.** Detail of compact bone showing radial microcracks (small white arrows). The cavities of Haversian canals can be empty (black arrow) or filled with pyrite framboids (large white arrow). **D.** Well preserved osteocyte cells (arrow) within the carbonate-rich fluoroapatite fossil bone. **E.** Globular lepidocrocite (arrows) in the bone matrix. All figures in plane polarized light except C which is cross polarized.

Fig. 6. Transmitted light photomicrographs and SEM images of petrographic thin sections showing different Ca-Mg-carbonate cements lining and filling cancellous bones. **A.** Whale bone trabeculae (wb) are lined and encrusted by thin rims (arrows) of microcrystalline dolomite and clotted dolomite (cd). Locally, micropeloids (mp) are associated with clotted dolomite which lines trabecular bones (boxed area). Sparry calcite (sc) occludes the voids. **B.** Detail (magnification of the boxed area in **A**) of an aggregate of micropeloids (arrows). The micropeloids are stained by opaque Fe-sulfides (py: pyrite) and -oxyhydroxides (lep: lepidocrocite) . **C.** High magnification of one micropeloid. Micropeloids consist of a microcrystalline dolomite nucleus (md) surrounded by small rhombohedral dolomite crystals (arrows). **D.** SEM image of one micropeloid with a rim of rhomoboedral dolomite crystals (arrow) lining bone trabecula (wb), and cemented with sparry calcite (sc). **E.** Detail of the micropeloid (high magnification of boxed area in **D**). Note the clotted

831 (3-5 μm) microcrystalline dolomite (md) and the well developed rhombohedra on the external part
832 (arrows). **F.** Pyrite framboids (py) partially oxidized into lepidocrocite (lep) and closely associated
833 with small rhombohedral dolomite (rd). Note the internal area of framboids with still preserved
834 pyrite microcrystallites. A, B, and C in plane polarized light.
835
836
837 **Fig. 7.** Transmitted light photomicrographs of petrographic thin sections showing rosette-like
838 cements lining whale bones. **A.** Rosette-like structures (white arrows) close to bone trabeculae and
839 embedded in sparry calcite. Rosette-like structures occur typically as isolated and paired bodies, or
840 in small aggregates. At the top note clotted dolomite (cd) embedded in the sparry calcite cement.
841 Note also the osteocytes (black arrow) within the whale bone. **B.** Detail of rosette-like structures
842 formed by few small pyrite framboids (py) surrounded by rhombohedral dolomite crystals.
843
844
845 **Fig. 8.** Raman spectra of the carbonate cements filling cancellous bones and of pyrite-lepidocrocite
846 framboids. **A.** Raman spectral signature of rhombohedral dolomite crystals and sparry calcite. **B.**
847 Raman spectral signature of pyrite and lepidocrocite minerals. Note the presence of well-defined D
848 (1350 cm^{-1}) and G (1600 cm^{-1}) peaks associated with both the dolomite crystals and pyrite,
849 indicating the presence of disordered carbonaceous matter (DCM).
850
851
852 **Fig. 9.** Transmitted light photomicrographs of petrographic thin sections showing Type 1
853 microborings in cancellous and compact bones. **A.** Trabeculae of cancellous bones (wb) intensely
854 bored by Type 1 microborings (arrows). Cancellous bones are filled with clotted dolomite (cd),
855 micropeloids (mp) and sparry calcite (sc). **B.** Detail of Type 1 microborings within trabecular

bones. They do not show any preferential orientation. **C.** Type 1 microborings in compact bone. This image shows an intensively bioeroded area (300 μm thick) which is tunneled with a pattern that follows the micro-architecture of the bone tissue. Note in fact that the bioeroded area is delimited by bright cement lines (arrows) that mark the boundaries between the secondary osteons of the Haversian systems. **D.** Detail of the intensively bioeroded compact bone. The Haversian canal contains a reddish lepidocrocite grain (arrow). Note that bioerosion totally obliterate the concentric lamellae typical of the osteons. All figures in plane polarized light.

Fig. 10. Transmitted light photomicrographs of petrographic thin sections showing Type 2 microborings in compact bones. **A.** Type 2 microborings on the external side of the compact bone. Note the 90° bifurcations (arrows). **B.** Detail of Type 2 microborings. Note the reddish lepidocrocite grains forming central swellings (small arrows) and a sack-shaped swelling at the tip of the same filament (large arrow). **C.** The arrow point to a bifurcating microboring containing two small reddish lepidocrocite grains which highlight internal segmentation. **D.** Bifurcating Type 2 microborings (small arrows). Note the large aperture linking one tunnel to the outside of the bone (large arrow). The black dotted line delimits the external side of the bone.

Fig. 11. SEM images of the bioeroded bones. **A.** External surface of compact bones showing a 200 μm thick zone intensively bioeroded by Type 1 microborings. **B.** Detail of Type 1 microborings in cancellous bones. The microborings resemble empty tunnels with micron-sized mineral grains encrusting the walls (arrows). **C.** EDX analysis of the micron-sized Fe-oxide grains arrowed in B. Both apatite in the bone and the Fe-oxide were detected in this analysis. **D.** Barite crust covering the external surface of bones. Note the intensely bioeroded bones. **E.** Detail of the barite crust showing

its massive microcrystalline habit. **F.** EDX analysis of the barite crust. Barite is associated with Sr-rich calcite. A and E were made in backscattered electron mode, C and D in secondary electron mode with an acceleration voltage of 15 kV.

Fig. 12. Stable isotope analyses of the carbonate cements inside and outside the Voghera whale fossil bones. Cross-plot of $\delta^{13}C$ and $\delta^{18}O$ values of dolomite filling cancellous bones (triangles), concretionary dolomite enclosing the bones (squares) and sparry calcite (rhombi).

Figure 1
Click here to download high resolution image

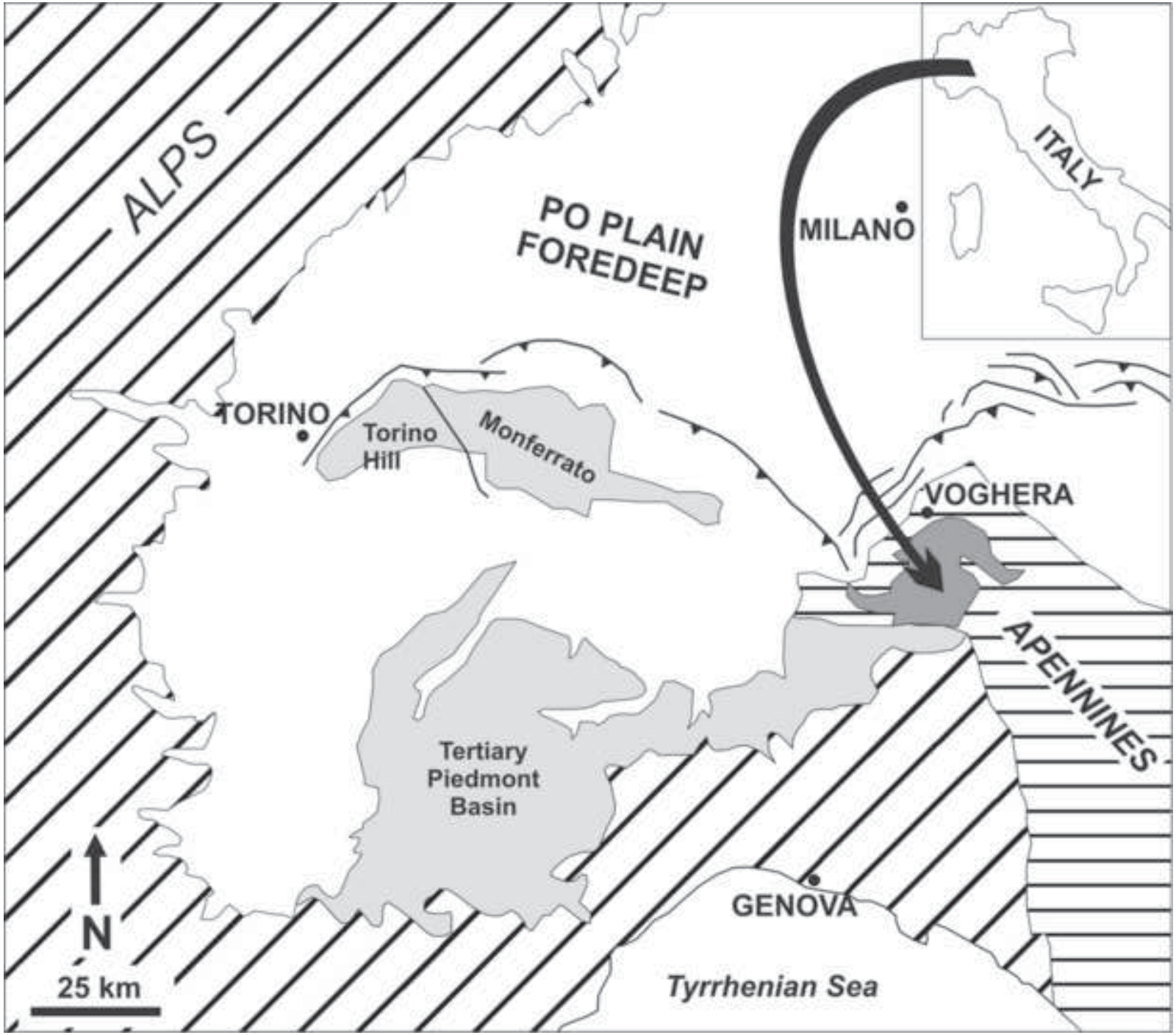

Figure 2
Click here to download high resolution image

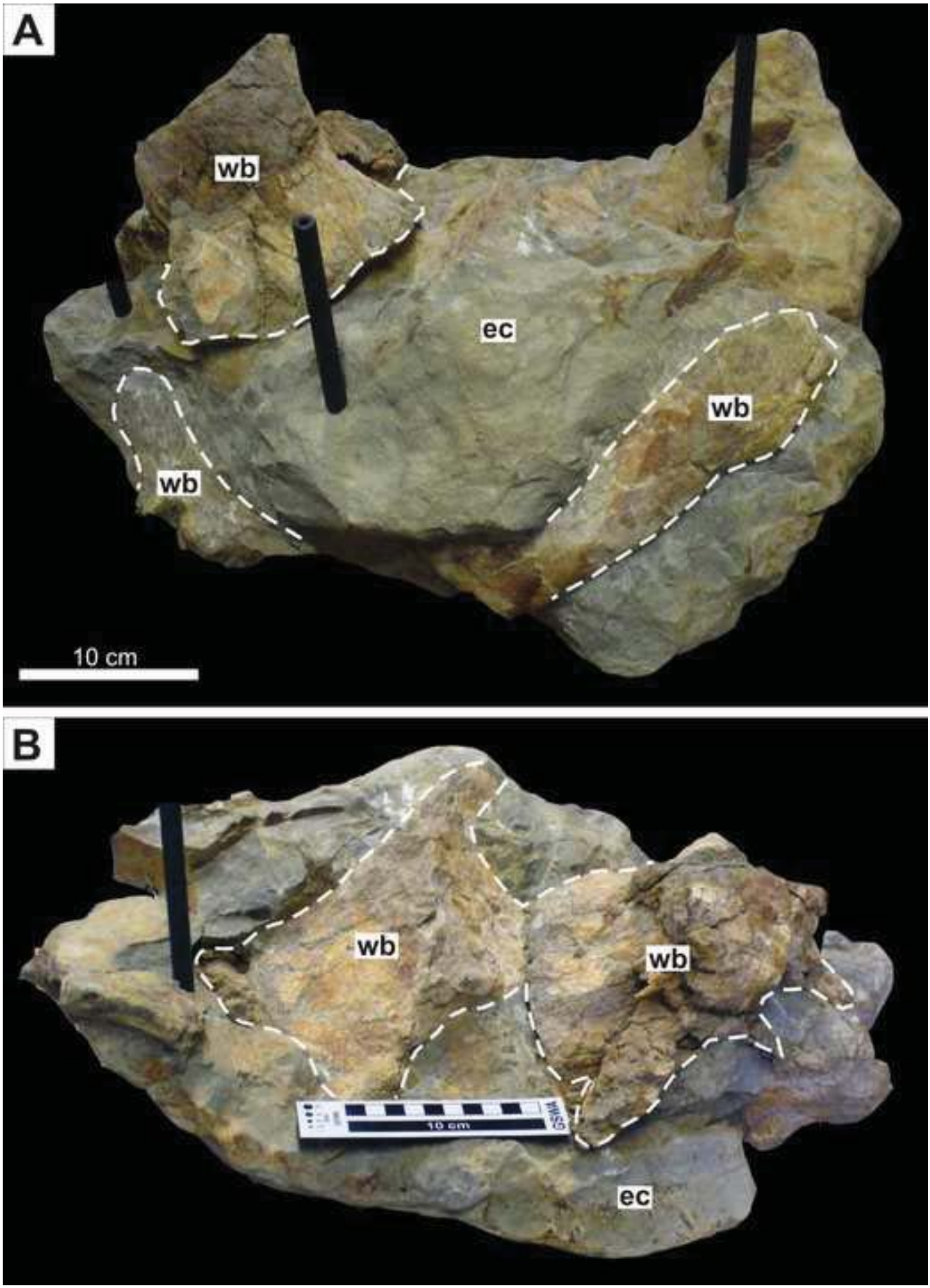

Figure 2 b&w
Click here to download high resolution image

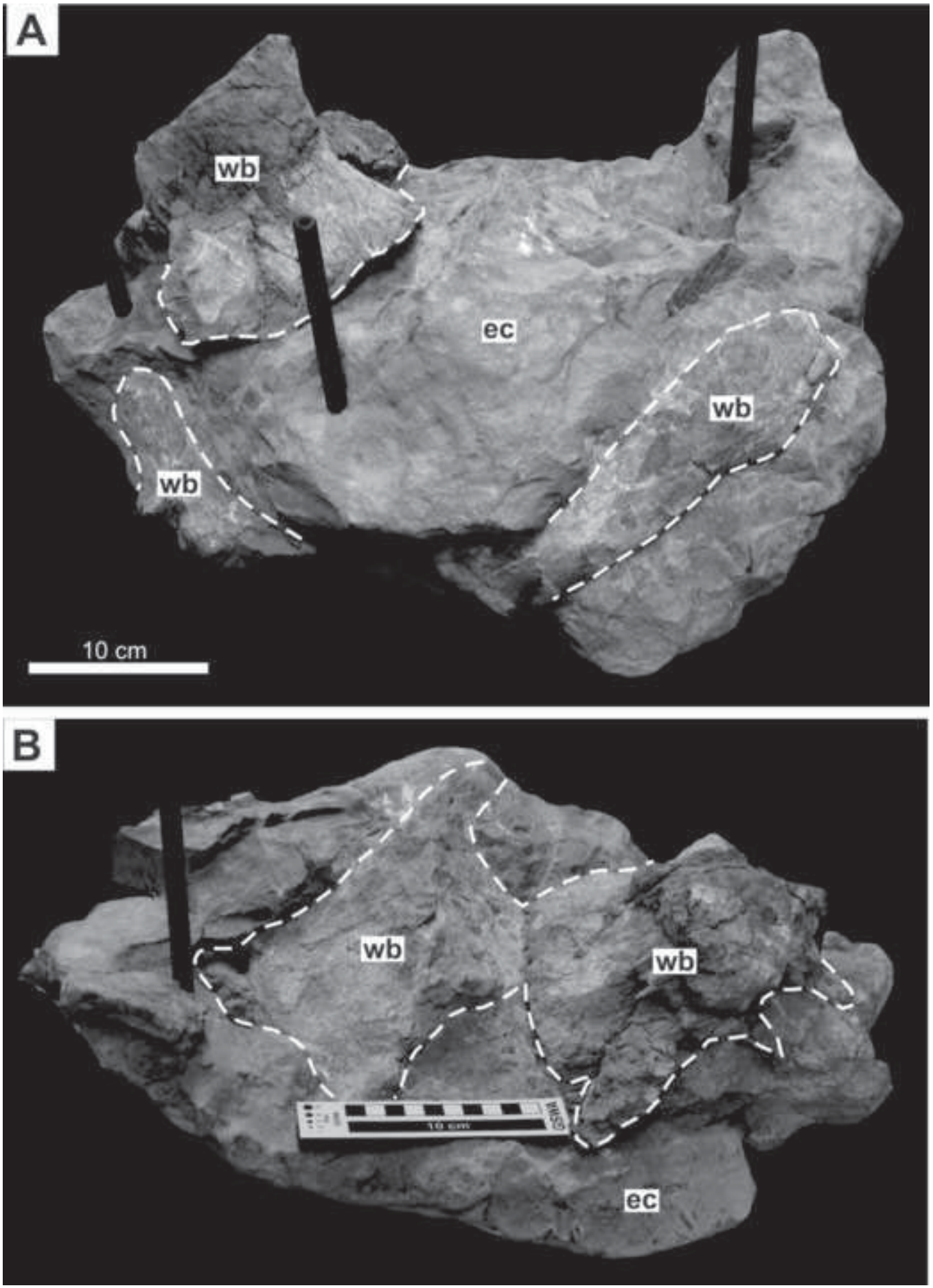

Figure 3
Click here to download high resolution image

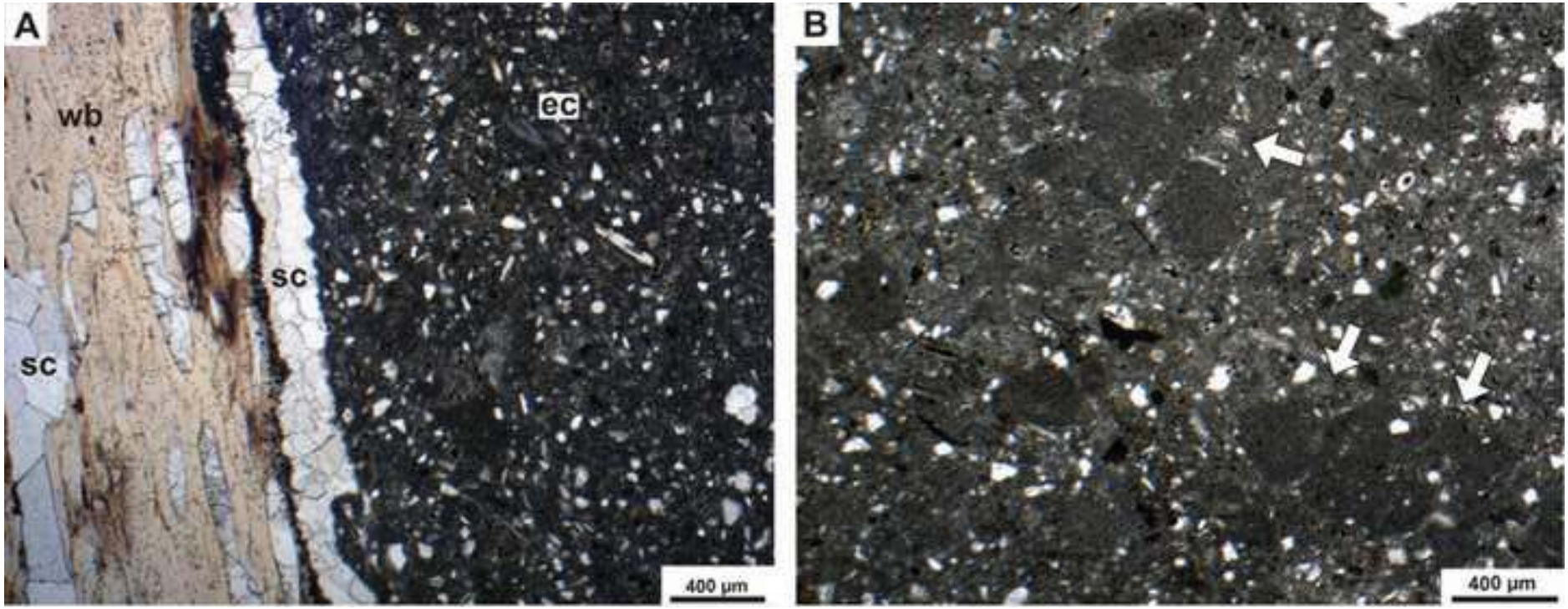

Figure 3 b&w
Click here to download high resolution image

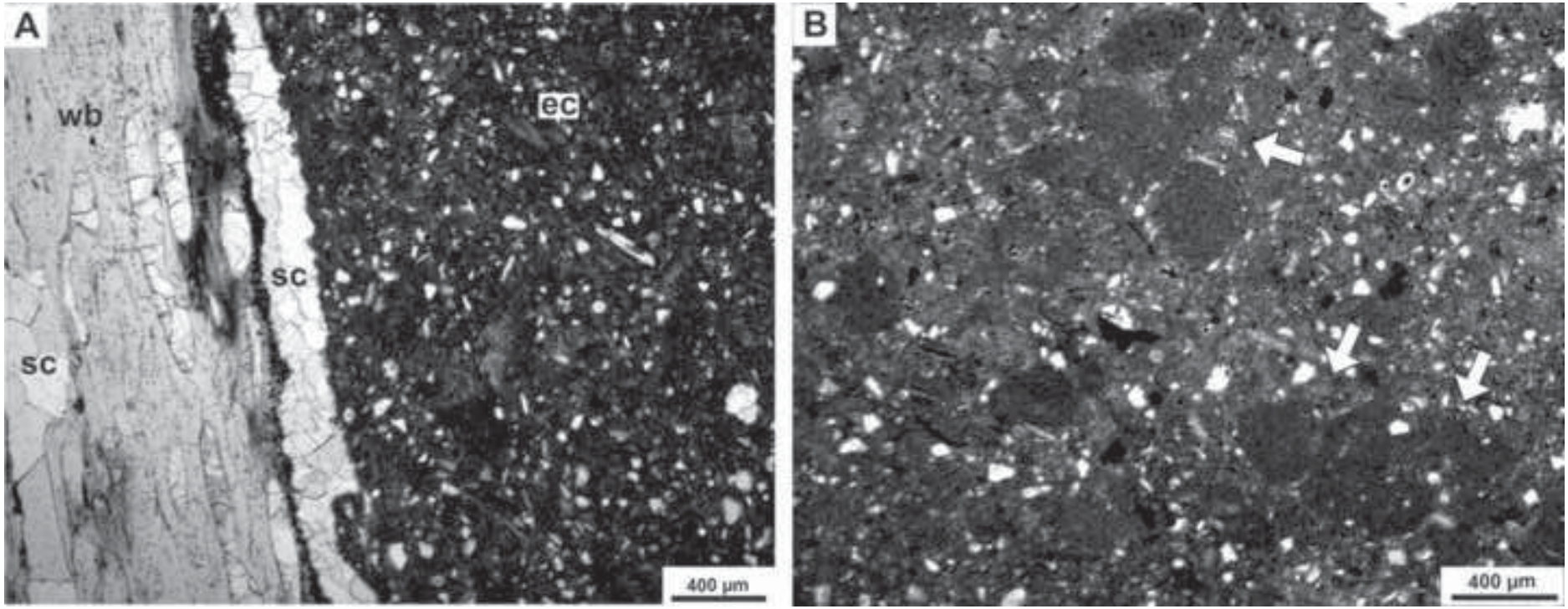

Figure 4
Click here to download high resolution image

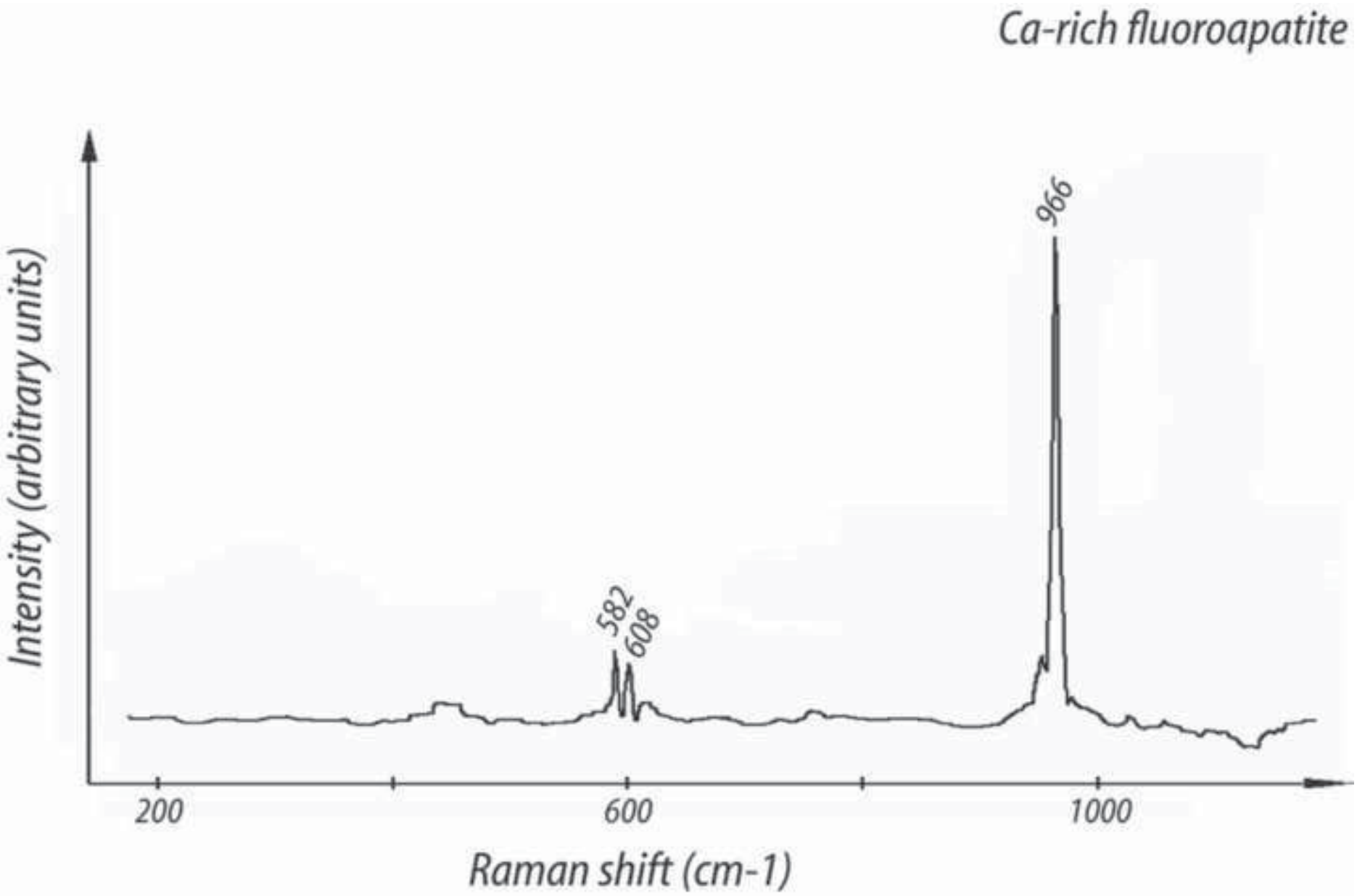

Figure 5
Click here to download high resolution image

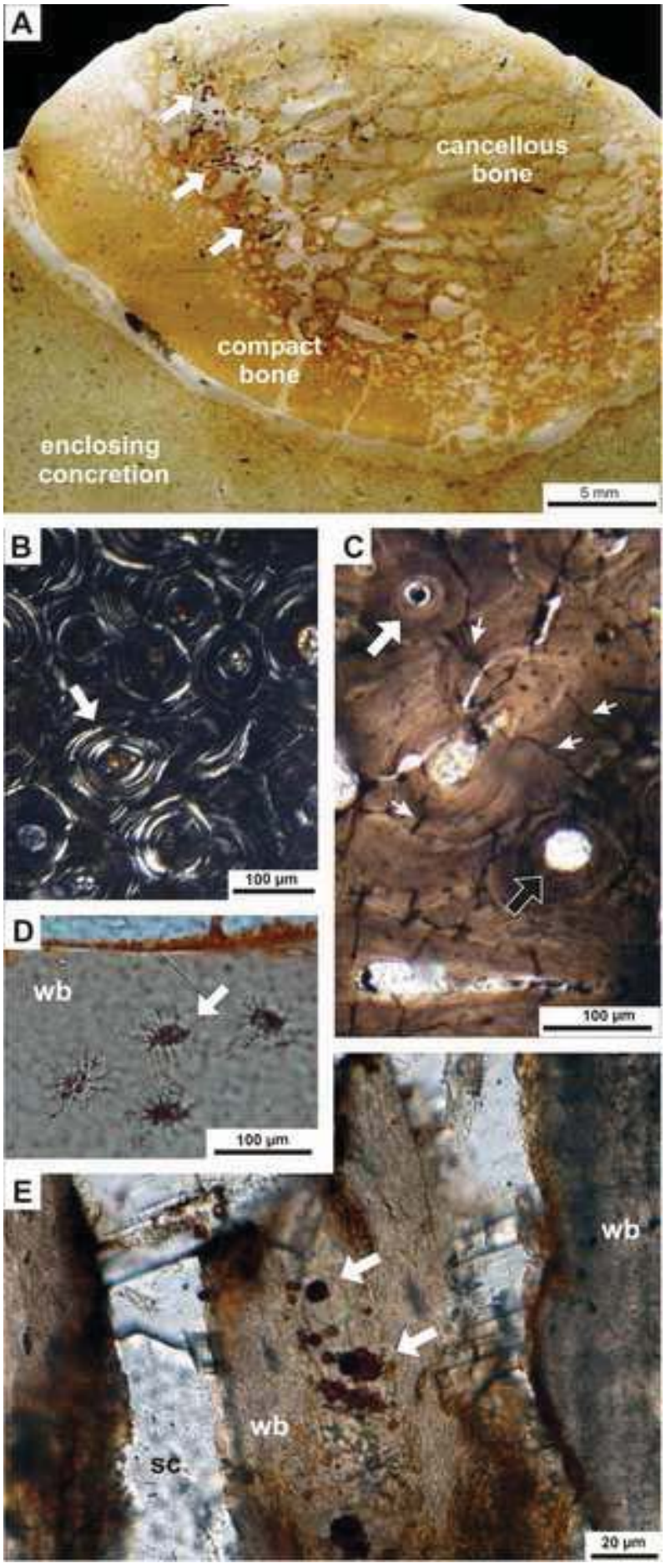

Figure 5 b&w
Click here to download high resolution image

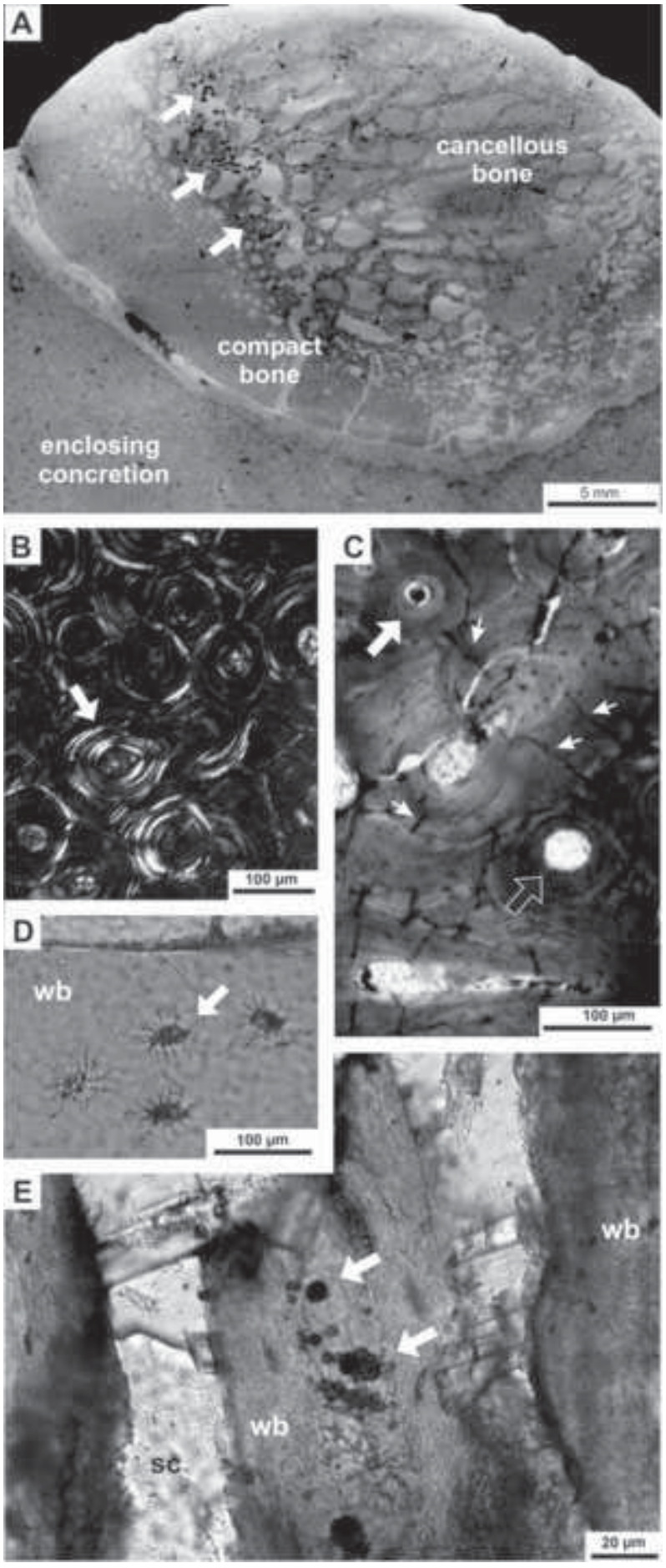

Figure 6
Click here to download high resolution image

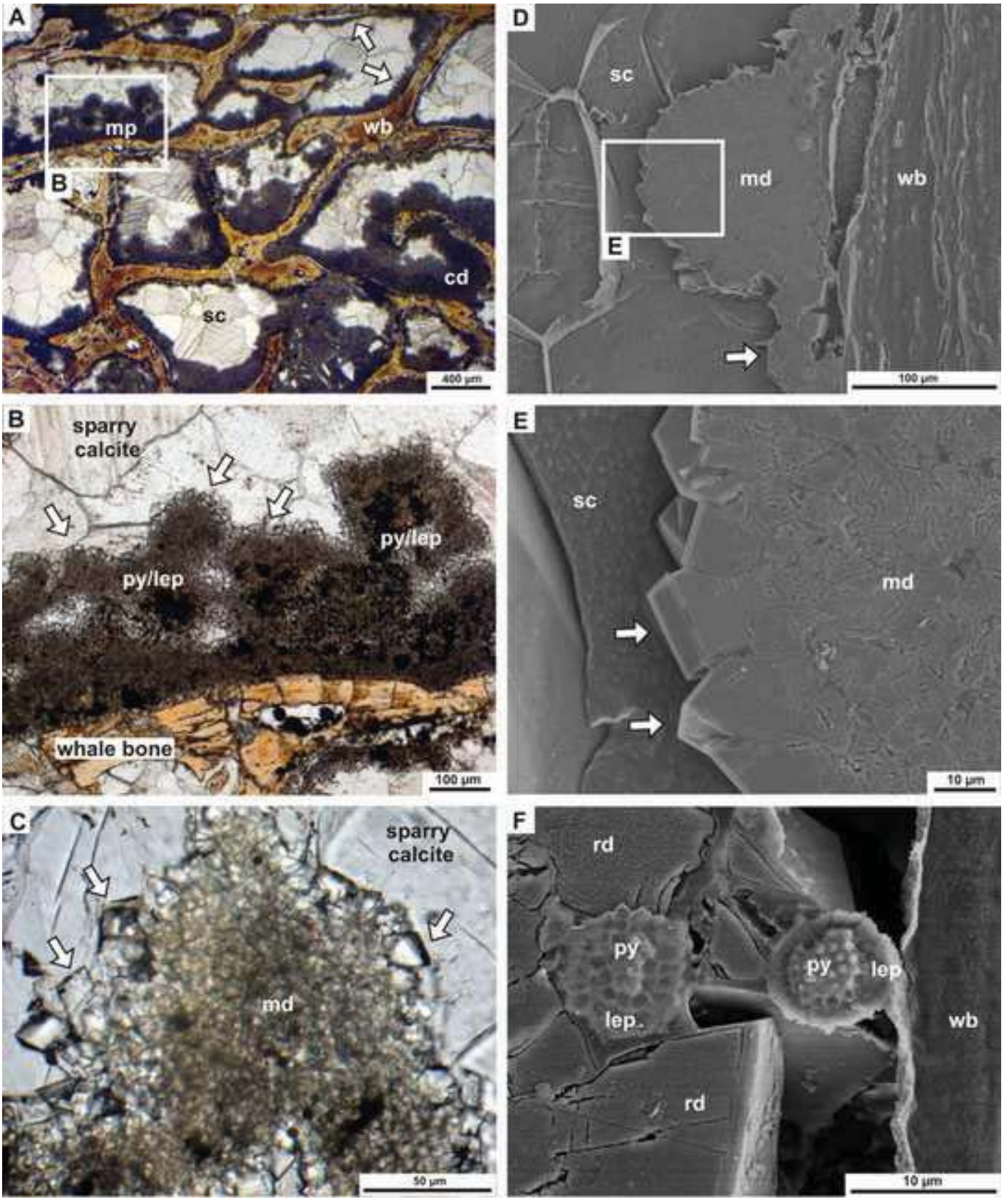

Figure 6 b&w
Click here to download high resolution image

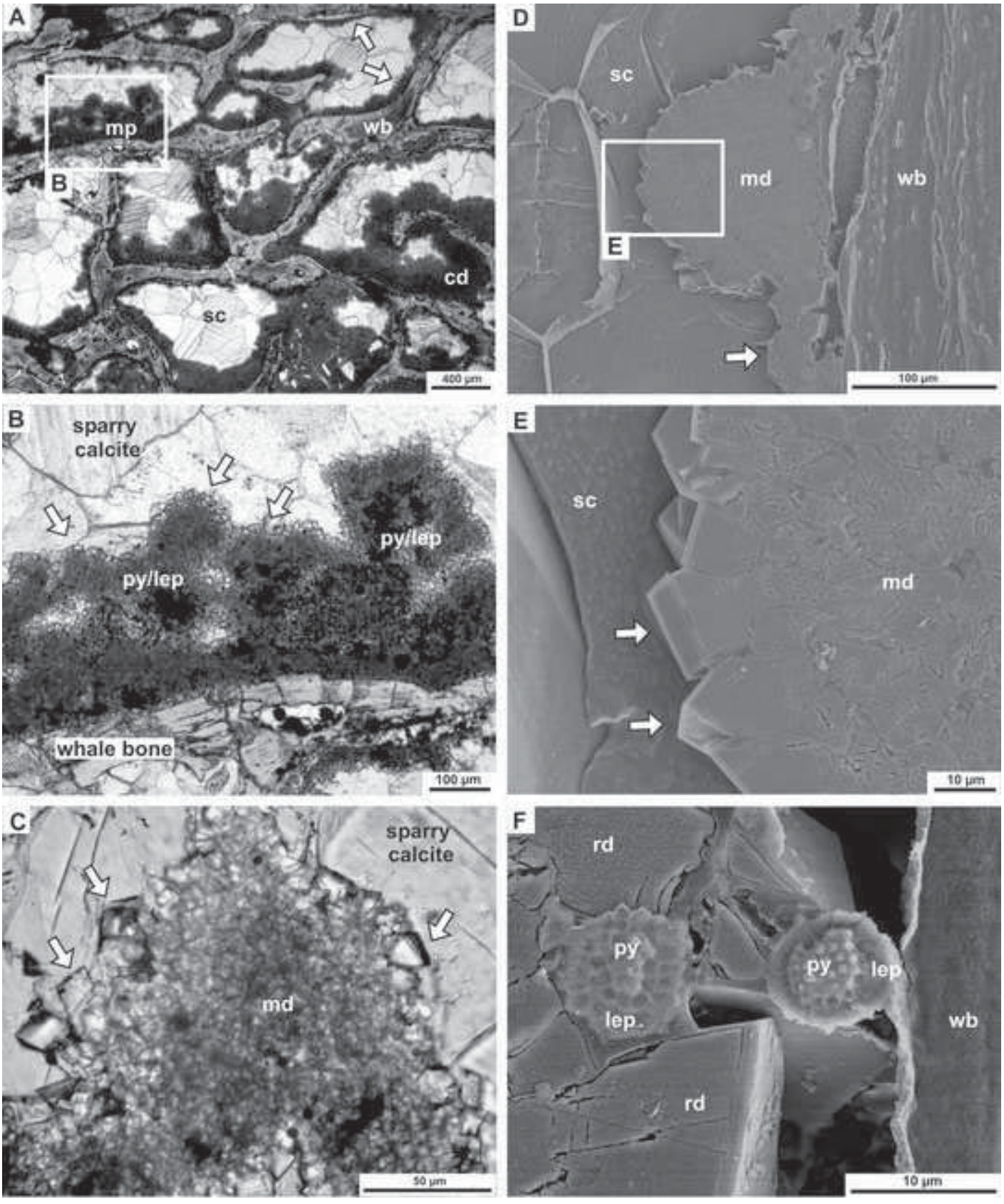

Figure 7
Click here to download high resolution image

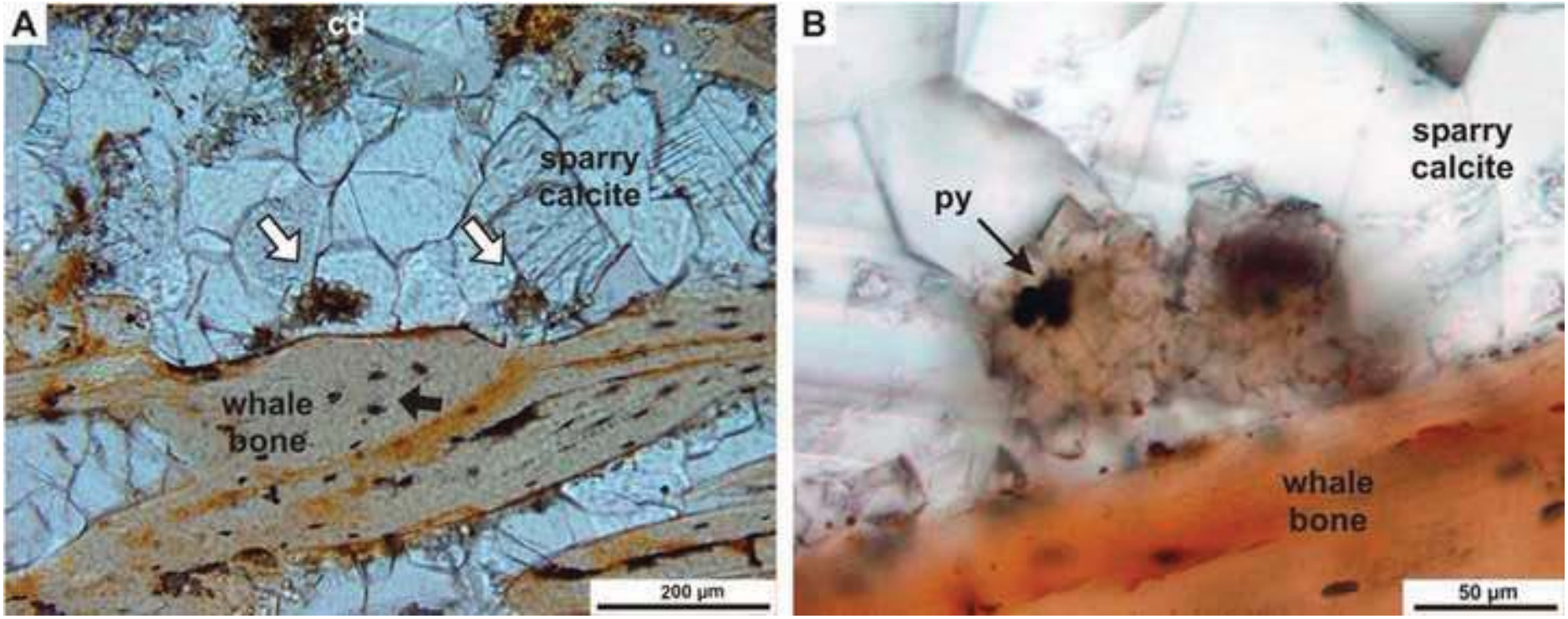

Figure 7 b&w
Click here to download high resolution image

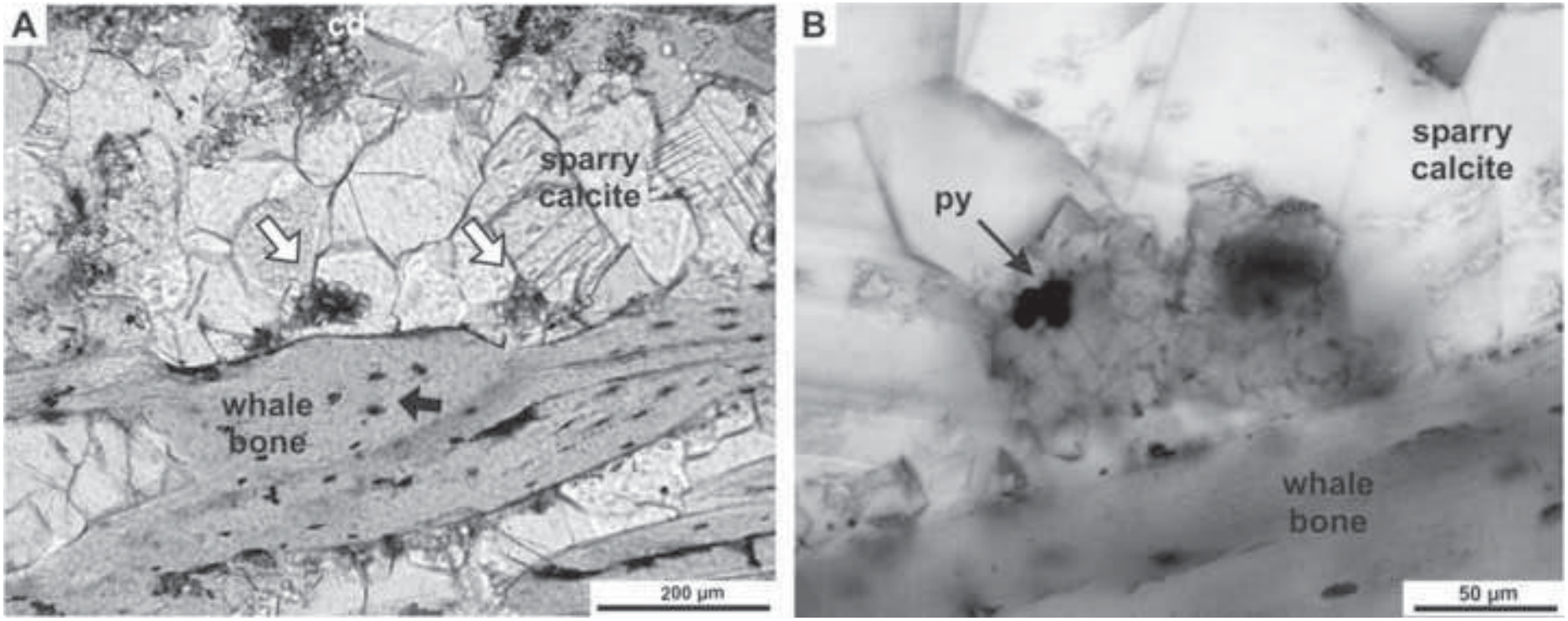

Figure 8

Click here to download high resolution image

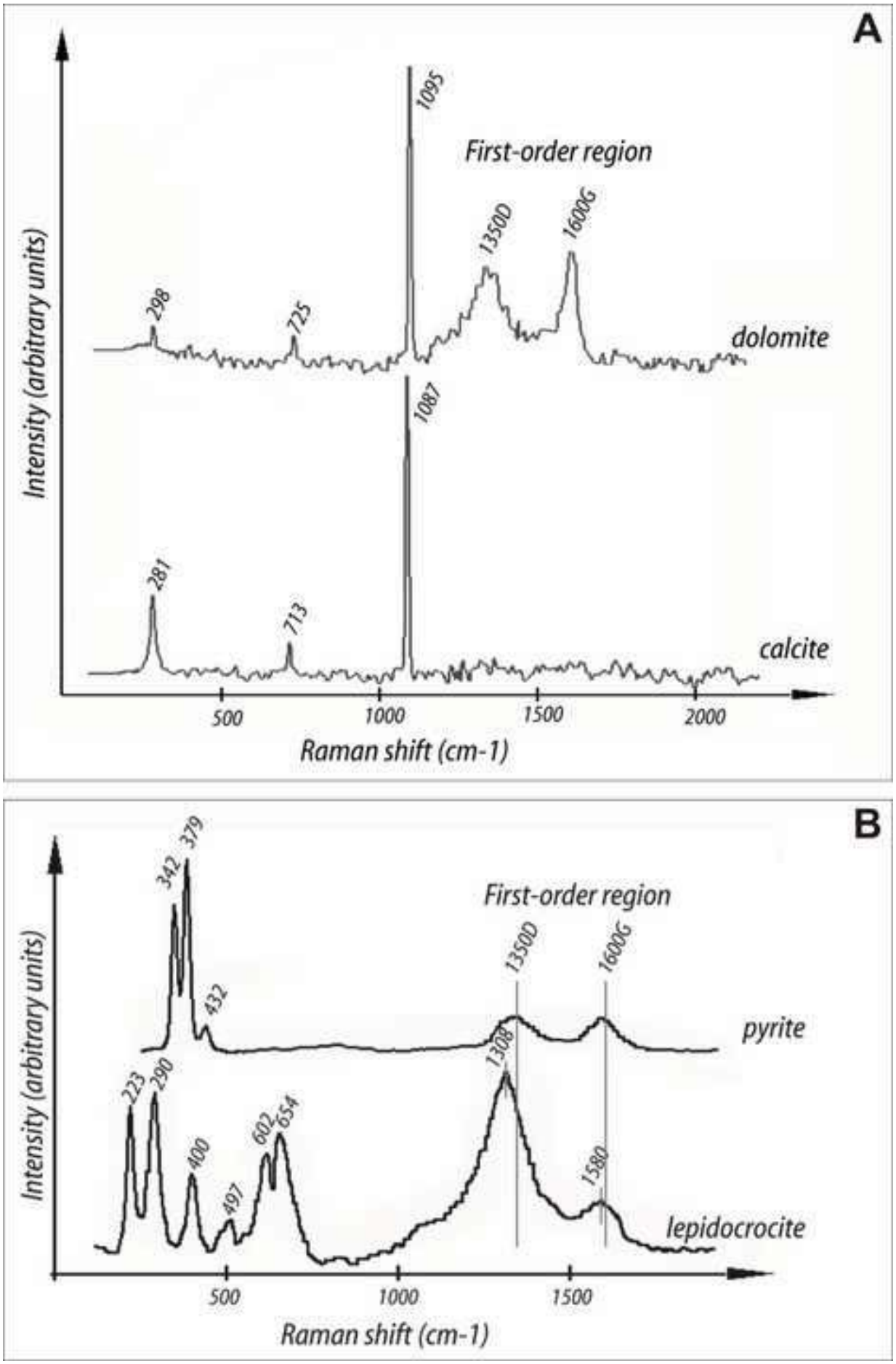

Figure 9
Click here to download high resolution image

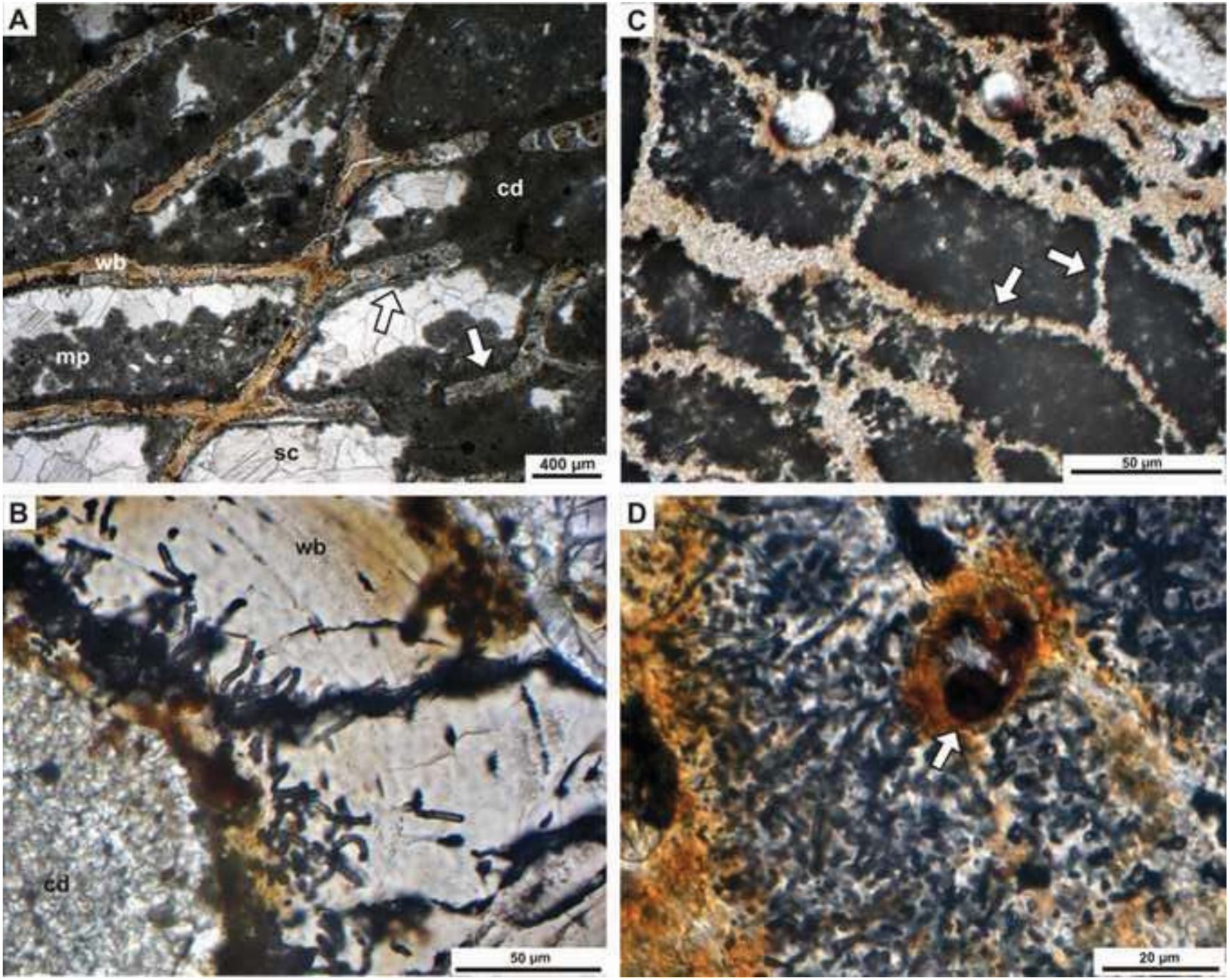

Figure 9 b&w

Click here to download high resolution image

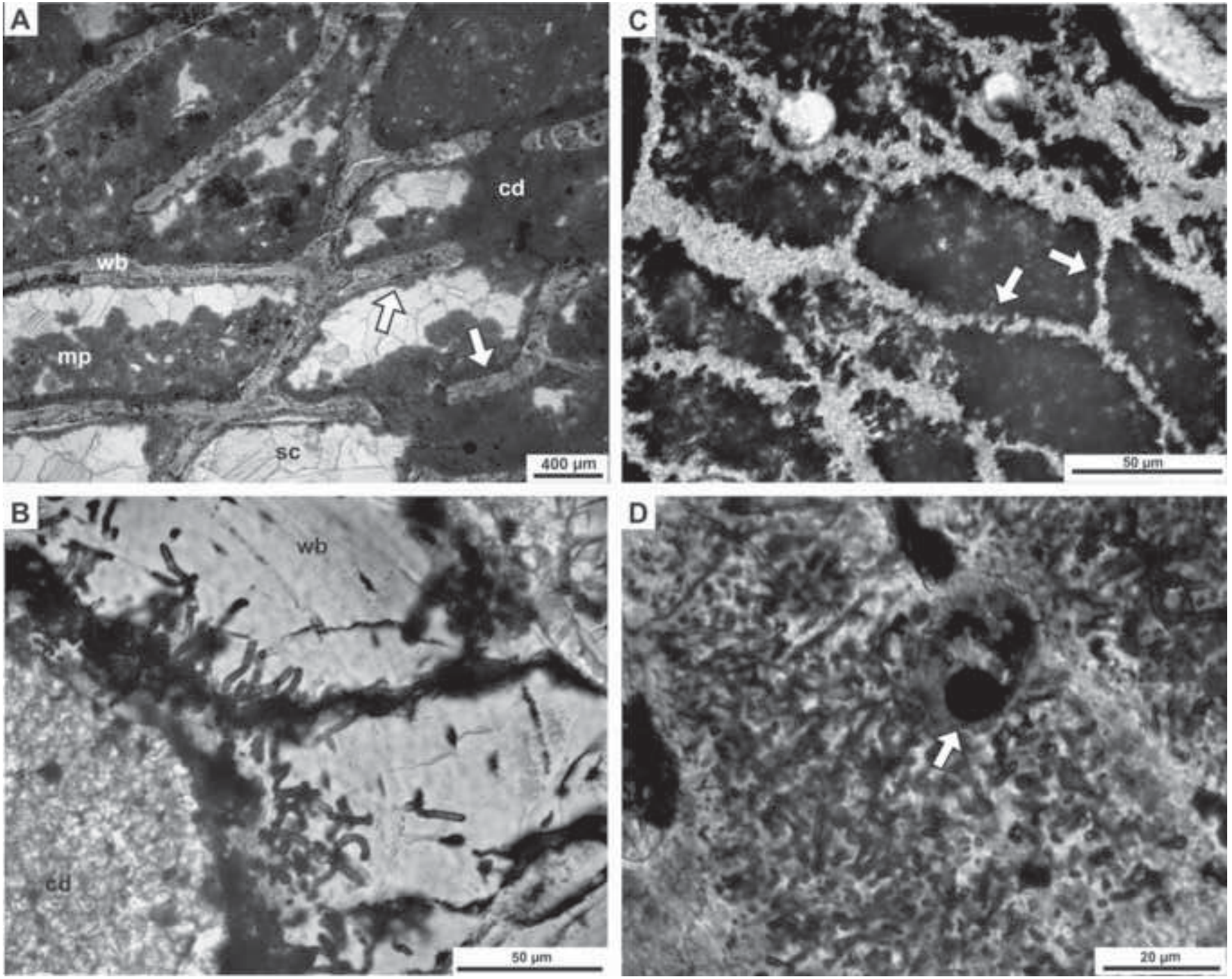

Figure 10

Click here to download high resolution image

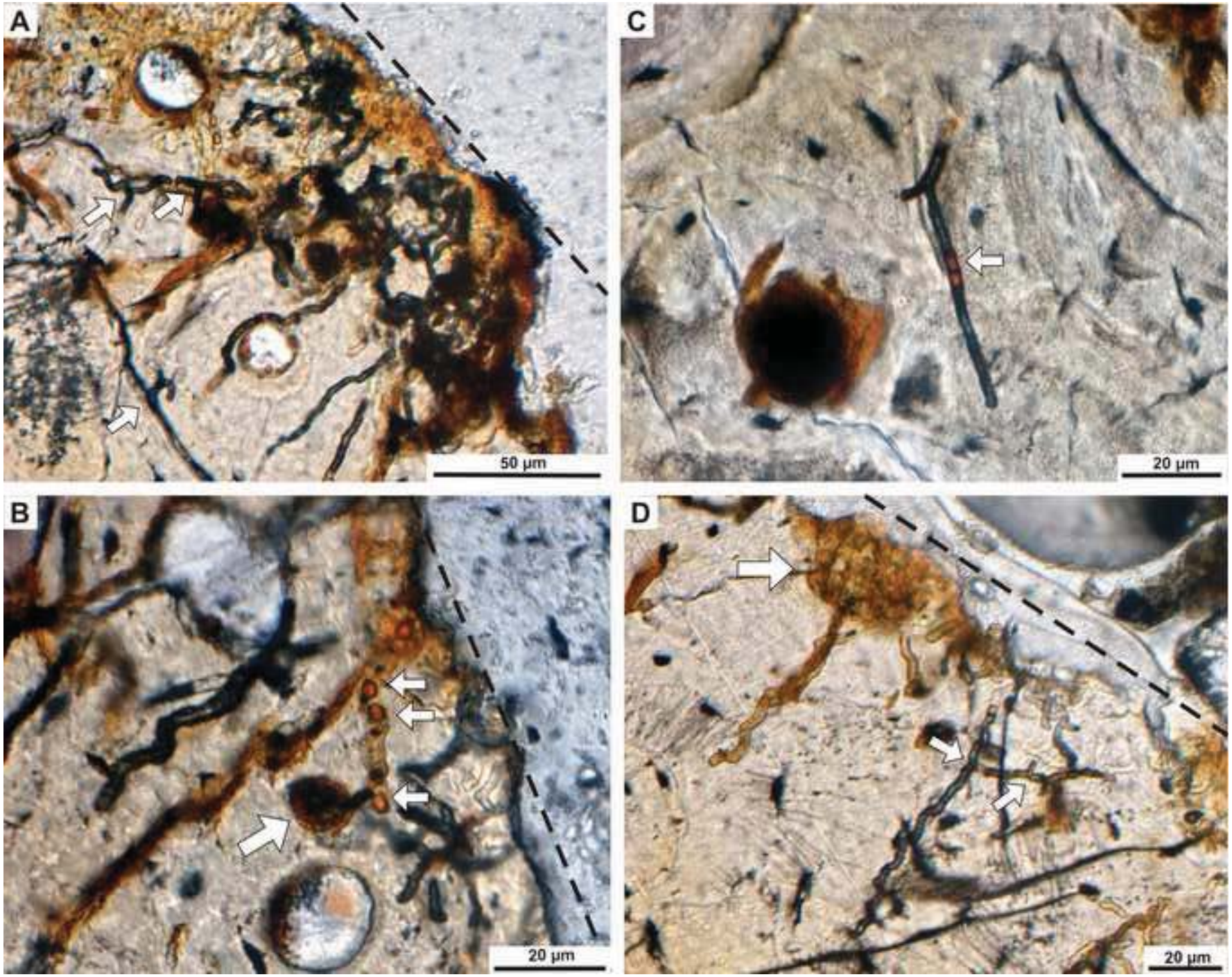

Figure 10 b&w

Click here to download high resolution image

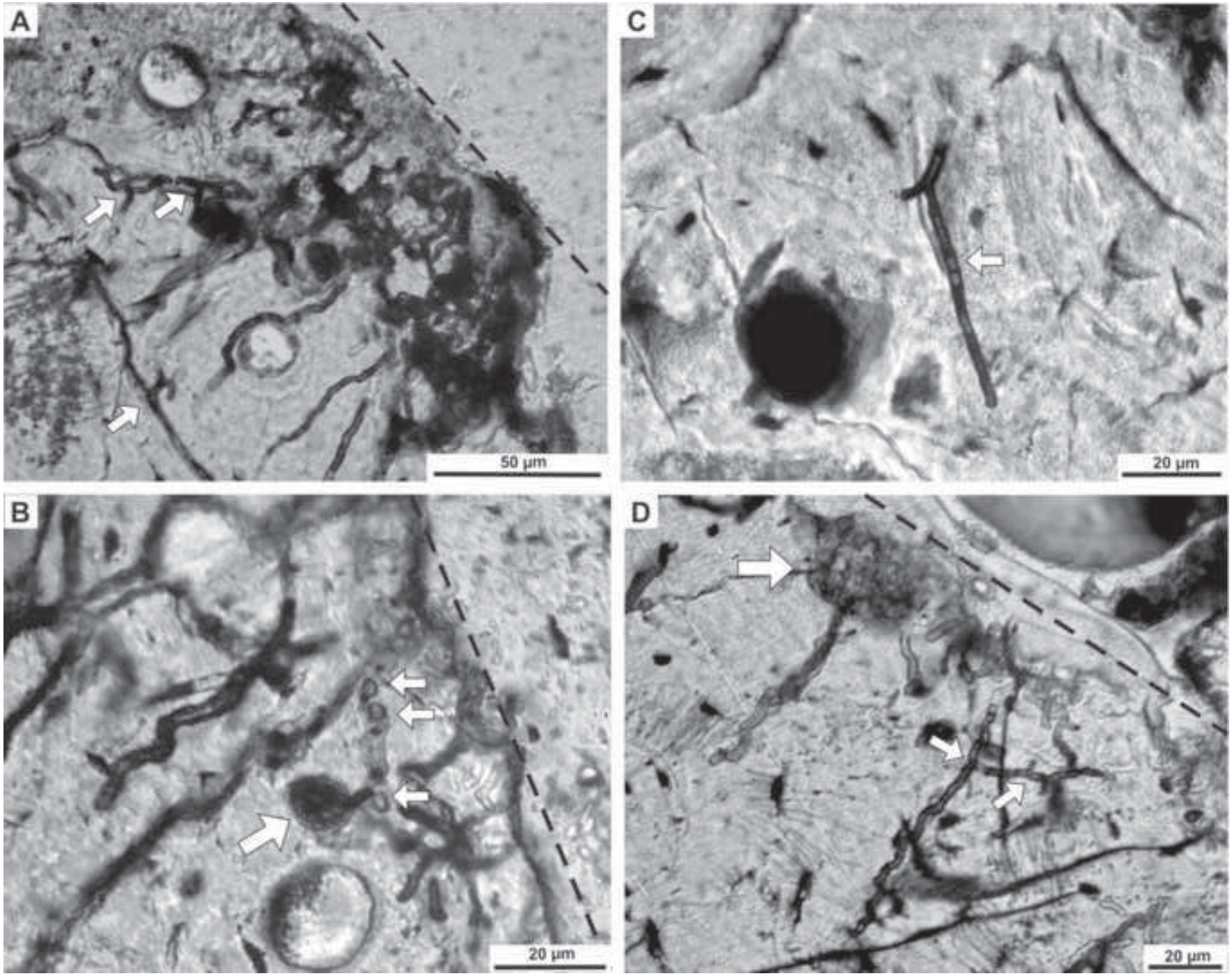

Figure 11

Click here to download high resolution image

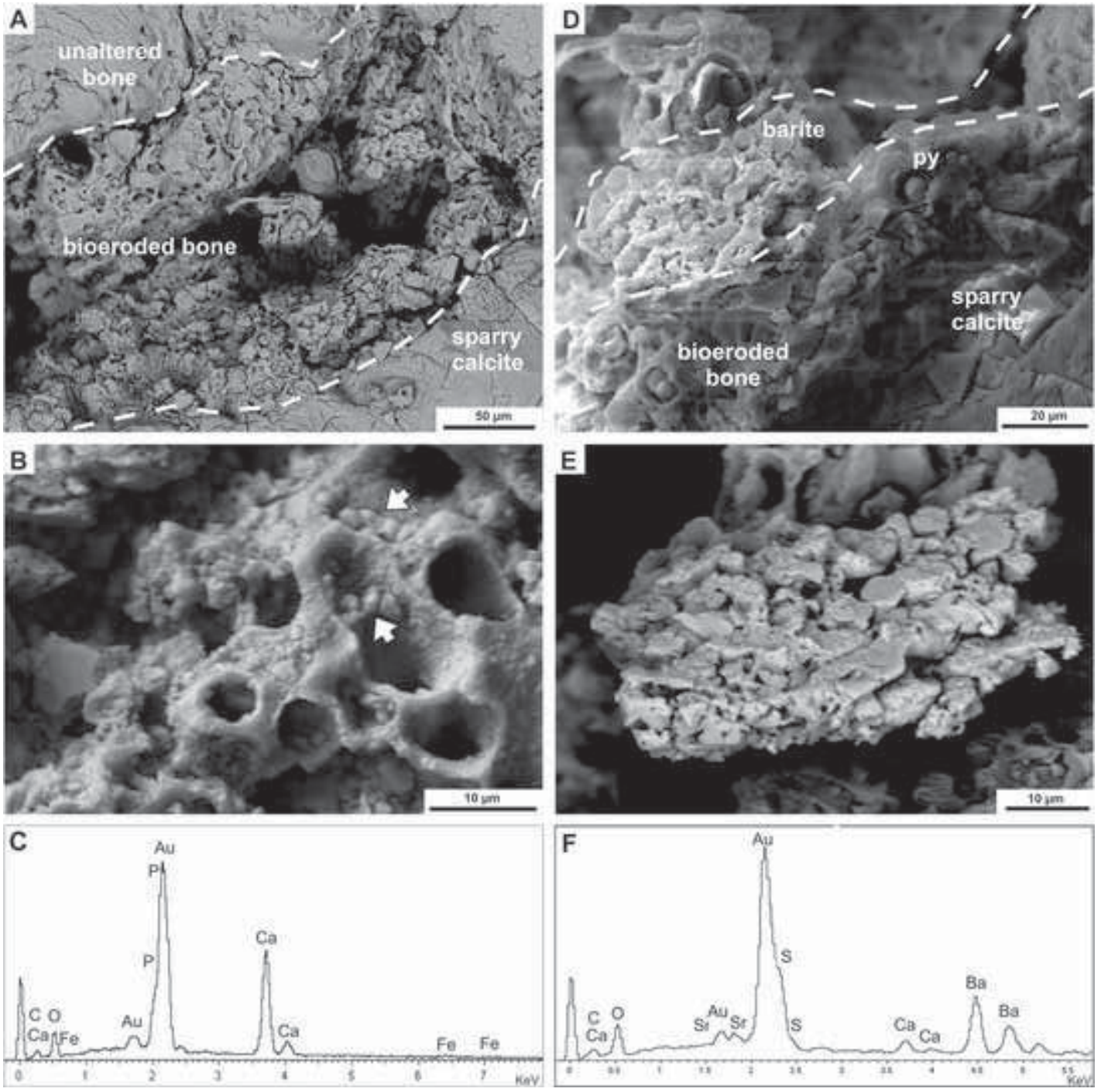

Figure 12
Click here to download high resolution image